

Article

CoFeBP Micro Flowers (MFs) for Highly Efficient Hydrogen Evolution Reaction and Oxygen Evolution Reaction Electrocatalysts

Shusen Lin , Md Ahasan Habib , Mehedi Hasan Joni, Sumiya Akter Dristy, Rutuja Mandavkar, Jae-Hun Jeong *, Young-Uk Chung *  and Jihoon Lee * 

Department of Electronic Engineering, College of Electronics and Information, Kwangwoon University, Nowon-gu, Seoul 01897, Republic of Korea; lss1187112907@gmail.com (S.L.); ahasanhabibbd1971@gmail.com (M.A.H.); mehedijs12001@gmail.com (M.H.J.); sdristy15@gmail.com (S.A.D.); rutuja.27rrm@gmail.com (R.M.)

* Correspondence: myloveofjh@gmail.com (J.-H.J.); yuchung@kw.ac.kr (Y.-U.C.); jihoonlee@kw.ac.kr (J.L.)

Abstract: Hydrogen is one of the most promising green energy alternatives due to its high gravimetric energy density, zero-carbon emissions, and other advantages. In this work, a CoFeBP micro-flower (MF) electrocatalyst is fabricated as an advanced water-splitting electrocatalyst by a hydrothermal approach for hydrogen production with the highly efficient hydrogen evolution reaction (HER) and oxygen evolution reaction (OER). The fabrication process of the CoFeBP MF electrocatalyst is systematically optimized by thorough investigations on various hydrothermal synthesis and post-annealing parameters. The best optimized CoFeBP MF electrode demonstrates HER/OER overpotentials of 20 mV and 219 mV at 20 mA/cm². The CoFeBP MFs also exhibit a low 2-electrode (2-E) cell voltage of 1.60 V at 50 mA/cm², which is comparable to the benchmark electrodes of Pt/C and RuO₂. The CoFeBP MFs demonstrate excellent 2-E stability of over 100 h operation under harsh industrial operational conditions at 60 °C in 6 M KOH at a high current density of 1000 mA/cm². The flower-like morphology can offer a largely increased electrochemical active surface area (ECSA), and systematic post-annealing can lead to improved crystallinity in CoFeBP MFs.

Keywords: water splitting; CoFeBP; micro flower; electrocatalyst; post-annealing



Citation: Lin, S.; Habib, M.A.; Joni, M.H.; Dristy, S.A.; Mandavkar, R.; Jeong, J.-H.; Chung, Y.-U.; Lee, J. CoFeBP Micro Flowers (MFs) for Highly Efficient Hydrogen Evolution Reaction and Oxygen Evolution Reaction Electrocatalysts.

Nanomaterials **2024**, *14*, 698. <https://doi.org/10.3390/nano14080698>

Academic Editor: Félix Zamora

Received: 22 March 2024

Revised: 11 April 2024

Accepted: 15 April 2024

Published: 17 April 2024



Copyright: © 2024 by the authors. Licensee MDPI, Basel, Switzerland. This article is an open access article distributed under the terms and conditions of the Creative Commons Attribution (CC BY) license (<https://creativecommons.org/licenses/by/4.0/>).

1. Introduction

Due to massive carbon emissions along with our heavy fossil fuel energy reliance, the globe is experiencing serious environmental issues and climate changes, such as unusual temperatures, super El Niño/La Niña, torrential rain, flooding, etc. It is urgently necessary to develop renewable green energy resources to address these global climate and environmental problems and also to meet future energy demands [1,2]. Hydrogen is one of the most promising green energy alternatives owing to its high gravimetric energy density, convenient usages, and zero-carbon emissions [1,3,4]. It can offer further advantages. For example, when the green hydrogen energy system is combined solar or wind power systems, the electricity supply can become more stable and optimized in terms of on-demand usage of electricity, easy storage, and convenient delivery. The demand of hydrogen has experienced substantial growth in the last 20 years with its utilization in power, transport, fuel cells, energy storage, and so forth, indicating large economic benefits [5]. Green hydrogen with zero-carbon emissions can be produced by water electrolysis, consisting of two half electrochemical reactions of hydrogen evolution reaction (HER) and oxygen evolution reaction (OER). Currently, the Pt-, Ir-, and Ru-based electrodes are the standard benchmark catalysts, but their high costs and low earth abundance restrict the large-scale adaptation of green hydrogen [3,4]. The development of highly efficient and cost-effective alternative electrocatalysts is essential at this point.

Transition metal (TM)-based electrodes in combination with non-metallic elements can offer promising electrocatalytic alternatives due to their excellent electrochemical properties with the abundance on earth [6–8]. The TMs, i.e., Co, Fe, Ni, Mn, etc., with un-filled d-orbitals can promote excellent water electrolysis capability and alkaline media stability and, thus, can be suitable for water electrolysis systems [9–11]. Among them, cobalt (Co) is one of most widely studied TMs due to the high adsorption and desorption rates for the reaction intermediates of the water-splitting (WS) process [12]. For instance, Co-Ni-P hollow nano-bricks exhibited low HER/OER overpotentials due to the abundant mass diffusion pathways and excellent catalytic functionalities [13]. Iron (Fe) is also an abundant TM, and Fe-contained compounds demonstrate high catalytic performances toward the HER/OER [14]. For example, Fe-Ni-Co nanostructures demonstrated low HER/OER overpotentials as well as low 2-electrode (2-E) cell voltage of 1.6 V at 10 mA/cm² due to the synergy between elements and high electrochemical active surface area (ECSA) [15]. Fe can demonstrate high selectivity for various hydrocarbons and oxygenates, which makes it promising for the application of electrochemical water splitting [15]. In terms of non-metallic elements, phosphorus (P) has been one of the most widely studied components in the last few decades [6,16]. The TM-P electrocatalysts can effectively alter the surface electrochemical properties and boost the WS catalytic reactions [6,16]. They also demonstrate the ability to modify the electronic structure by adjusting the oxidation states and electron density, which can further improve the efficiency in promoting both HER/OER reactions [17]. For instance, the Co₃O₄P nanowires/NF demonstrated superior HER efficiency and bifunctional ability in 1.0 M KOH [18]. The induced positive charged sites on the surface can enhance the adsorption of OER intermediates such as OOH* and O*, which potentially boost oxygen generation [18]. More recently, boron (B) has been gaining increased attention as another non-metallic element for TM-based electrocatalysts. TM-B-based electrocatalysts can effectively lower the kinetic energy barrier for the HER/OER and also offer superior electrochemical stability with the efficient orbital hybridization with the TMs [19–22].

To this end, the combination of Co, Fe, B, and P together in a high ECSA morphology can be a viable approach to develop an advanced electrocatalyst for highly efficient water electrolysis, along with their synergy and lower cost. In this work, a quaternary CoFeBP micro-flower (MF) electrocatalyst is demonstrated by a hydrothermal synthesis approach on a porous nickel form, as illustrated in Figure S6. The best optimized CoFeBP MF demonstrates comparable 3-electrode (3-E) and 2-E water electrolysis performances, as compared to the benchmark electrodes of Pt/C and RuO₂. For example, the CoFeBP MFs demonstrate low 3-E HER/OER overpotentials of 20 and 219 mV at 20 mA/cm² and low 2-E cell voltage of 1.60 V at 50 mA/cm². The improved performance can be linked to the high ECSA offered by the micro-flower (MF) morphology and synergy between the elements utilized. Also, systematic synthesis optimizations and vacuum annealing treatment can effectively reduce the point defects and improve the crystallinity of MFs, further facilitating the electrocatalytic effectiveness of electrocatalysts.

2. Electrode Fabrication and Structural Analysis

2.1. Precursor and Reaction Parameter Optimizations for CoFeBP MF

To begin with, porous Ni foam was adapted as the substrate due to excellent conductivity and porosity for CoFeBP micro-flower (MF) synthesis, and more details about the substrate and other preparation can be found in the Supplementary Text S1.1 and Figures S1–S5. Then, a CoFeBP micro flower (MF) was fabricated by a hydrothermal reaction on Ni form, followed by annealing optimization, as illustrated in Figure S6. Various hydrothermal reaction parameters were systematically optimized, and the best-optimized sample was taken for further annealing optimization. Various hydrothermal reaction parameters and precursor concentration optimization-related data are presented in Supplementary Section S2. Hydrothermal reaction duration and temperature were optimized as seen in Figures S7–S10, and the best-optimized sample at 140 °C for 8 h was taken for further optimization. The

elemental ratio of B-P was optimized, as seen in Figures S11–S13. The Co and Fe concentration was optimized in a total molarity of 2 mM, as seen in Figures S14–S16, where the Co₉₀-Fe₁₀-B₅₀-P₅₀ (1.8 mM Co and 0.2 mM Fe and 6 mM of B and P) demonstrated the best HER/OER performances with overpotentials of 204 and 462 mV at 200 mA/cm², as summarized in Figure S16. The precursor ratio affects the atom aggregation, nucleation, and particle growth and, thus, is critical for the surface morphology, grain size, defect formation, and crystallinity [23]. An optimal elemental ratio is important as the O* and OH* absorption energy can be tuned along with different ratios [24]. The more detailed fabrication process of CoFeBP micro flowers (MFs) can be found in the Supplementary Text S1.5. In addition, the surface modifiers such as urea (CH₄N₂O) and ammonium fluoride (NH₄F) are adapted, as seen in Figures S17–S20. The addition of surface modifiers can be an effective approach to modify the nucleation process for high ECSA surface morphology [25–28]. For instance, the NH₄F can effectively tailor surface morphology and can help form 3D structures. The presence of F[−] ions (NH₄F → NH₄⁺ + F[−]) can readily chemisorb elements with dangling bonds and promote the nucleation process [29]. As a result, much more pronounced MF morphologies with thicker branches were commonly observed with the NH₄F inclusion, as seen in Figure S19. The urea₉₀-NH₄F₁₀ showed the best HER/OER overpotentials of 191 and 456 mV at 200 mA/cm² in the set, as summarized in Figure S20.

2.2. B-P Concentration Optimization for CoFeBP MF

Figure 1 shows the CoFeBP MF electrode fabrication with the B-P concentration variation. The ratio of boric acid (H₃BO₃) and sodium hypophosphite (H₂NaO₂P) was systematically controlled at a fixed total molarity of 12 mmol (mM). Other precursors were fixed at 1 mM Co(NO₃)₂•6H₂O for Co and 1 mM Fe(NO₃)₃•9H₂O for Fe based on the previous parameter optimizations. Along with the B-P concentration control, various surface morphologies of CoFeBP structures were observed, as seen in Figure 1a–e. Generally, the ternary CoFeB or CoFeP showed cluster morphologies, as seen in Figure 1a,e. Then, the quaternary CoFeBP electrodes showed 3D micro-flower (MF)-like morphologies, as seen in Figure 1b–d. The B₅₀-P₅₀ sample demonstrated the most well-defined MF morphology with the high-density branch structures along with the well-balanced elemental ratio of B and P, as seen in Figure 1c [30]. Due to the existence of five valence electrons in the outer shell of phosphorus (3s²3p³) [31] and high affinity of boron [32], strong ionic bonding with the metallic Co and Fe can be achieved through orbital hybridization with the well-balanced B and P. Additional SEM images can be found in Figure S11. The EDS phase maps of CoFeB₅₀P₅₀ MFs confirmed the uniform distributions of Co Lα1, Fe Lα1, B Kα, P Kα1, and Ni Lα1, as seen in Figure 1f–f-5. Also, the EDS spectrum of B₅₀-P₅₀ confirmed the presence of Co Lα1, Fe Lα1, B Kα, P Kα1, and Ni Lα1 peaks in Figure 1g. EDS spectra of other samples can be found in Figure S12. Atomic (At.) % summary in Figure 1h confirms the gradual increase in P incorporation along with the increased P (0–12 mM), while the Co, Fe, and B showed gradually decreasing trends. For the CoFeB₅₀P₅₀ MF, 25.79 and 30.82% of B and P atoms were incorporated and 29.29 and 10.57% of Co-Fe atoms were observed.

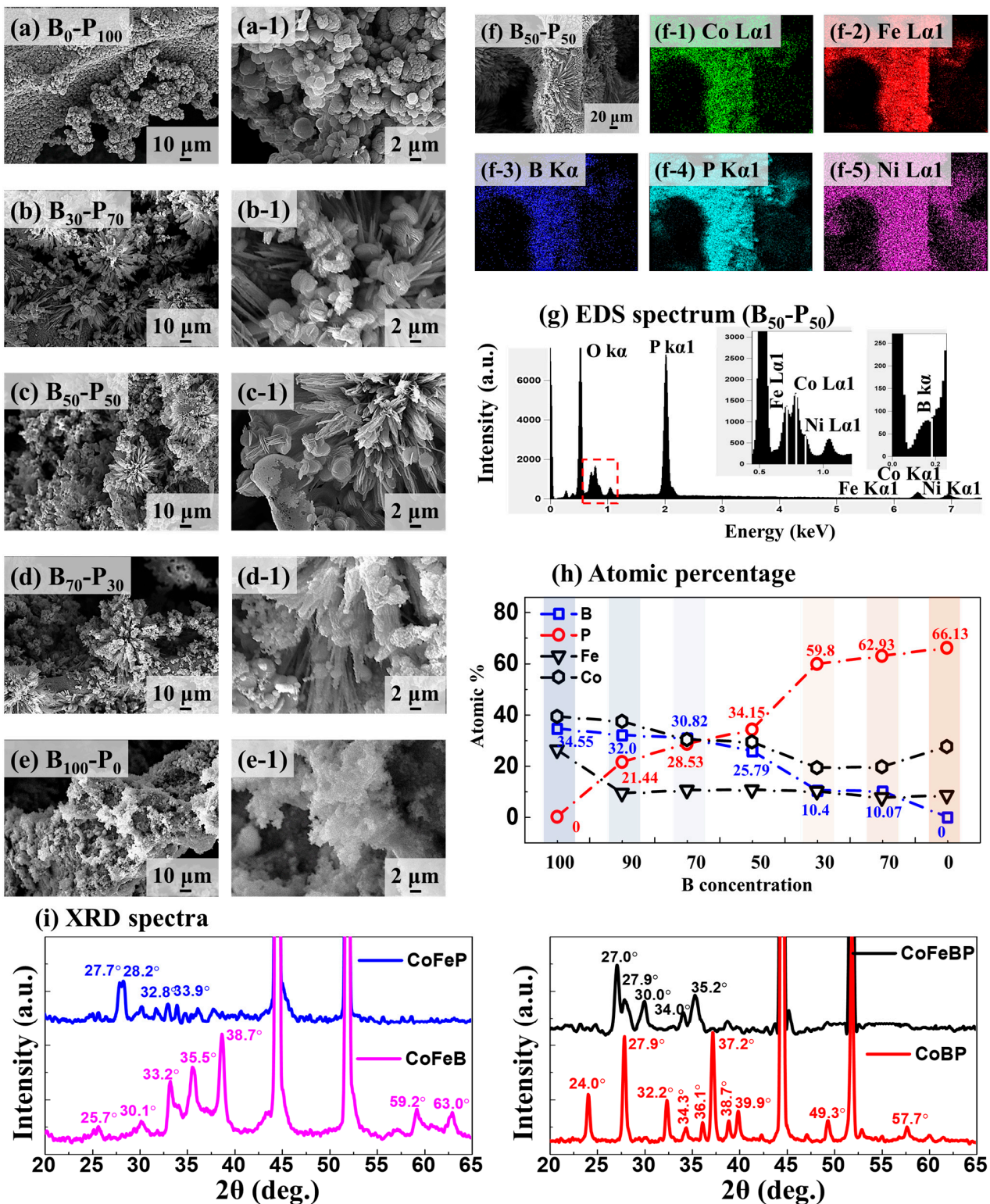


Figure 1. CoFeBP electrode fabrication with B-P concentration variation. Total molarity of B and P was fixed at 12 mM: B₅₀-P₅₀ indicates 6 mM B and P, namely CoFeB₅₀P₅₀. Other parameter variations can be found in the Supplementary Text. (a–e) SEM images of CoFeBP electrodes as labeled. (a–1–e–1) Corresponding enlarged SEM images. (f–f–5) SEM image of B₅₀-P₅₀ and corresponding EDS phase maps of Co Lα1, Fe Lα1, B Kα, P Kα1, and Ni Lα1. (g) EDS spectrum of CoFeB₅₀P₅₀. (h) Atomic percentage summary plots of Co, Fe, B, and P. (i) XRD spectra of CoFeBP, CoBP, CoFeP, and CoFeB electrodes.

The X-ray diffraction (XRD) of CoFeB, CoFeP, CoBP, and CoFeBP electrodes is shown in Figure 1i, and the individual XRD patterns of CoFeB, CoFeP, CoBP, and CoFeBP are shown in Figure S33. The XRD PDF cards of related compounds are shown in Figure S34. Two strong diffraction peaks were commonly observed at ~ 43 and 52° in all XRD patterns, which can be indexed to the (111) and (200) planes of the Ni foam substrate [33]. The polycrystalline phase was indicated with multiple diffraction peaks that did not show a match with the relevant combinations, such as Co-B, Co-P, Fe-B, Fe-P, and B-P. In detail, CoFeP exhibited strong peaks at 27.7 and 28.2° , and CoFeB possessed several intense peaks at 33.2 , 35.5 , and 38.7° and other secondary peaks. CoBP demonstrated stronger diffraction peaks at 27.9 , 32.2 , and 37.2° and other smaller peaks, which might indicate that CoBP is in a short-range polycrystalline phase [34]. The CoFeBP electrode showed slightly lower intensity and peaks at 27.0 , 27.9 , 34.0 , and 35.2° , which also indicate a polycrystalline phase [35]. Among the 2θ range from 20 to 65° , the appearance of multiple peaks in all samples might indicate the fabrication of polycrystalline structures [36]. Notably, recent studies suggested enhanced intrinsic water-splitting (WS) activity with the polycrystalline phase, as compared to the single-crystal structures due to the increased exposure of active sites and structural stability [22,35,37]. The long-range disordered polycrystalline surface can demonstrate higher structural flexibility and stability for the water-splitting reactions [22,35,37]. A more detailed discussion of the XRD analysis can be found in Supplementary Text S1.7.

2.3. Structural Analysis of CoFeBP MF along with Post-Annealing Optimization

Figure 2 shows the CoFeBP MFs along with the post-annealing temperature optimization on the best CoFeBP MFs after the synthesis parameter optimizations. The best CoFeBP MFs, i.e., Co₉₀-Fe₁₀-B₅₀-P₅₀ electrode, were taken for annealing in a rapid thermal processing (RTP) system, and a series of annealing experiments was conducted to establish the optimal conditions, as seen in Supplementary Text S2.3. The optimal annealing duration was 30 min based on the optimization study between 10 and 60 min, as seen in Figures S21 and S22. Along with the post-annealing temperature variation, there was no obvious change in the surface morphology below 200°C , as clearly seen in Figure 2a,b, and the MF morphology was well maintained. At 300°C , the branch structure began to fall off from the MF matrix, as shown in Figure 2c. At 500°C , severe structural damage were observed, i.e., branches were cracked due to the excessive thermal energy, as seen in Figure 2d [38]. Often, the electrocatalysts synthesized by the hydrothermal reaction can be in the polycrystalline phase [30], and the degree of crystallinity can be improved to a certain extent by moderate post-annealing treatment through adatom diffusion [30]. The charge transfer process can be promoted along with improved local crystallinity [38]. Annealing can improve the local crystallinity due to the removal of defects [39]; however, a longer duration or excessive temperature can exhibit structural damage [39]. The EDS phase maps of 100°C MF show the uniform distribution of Co L α 1, Fe L α 1, B K α , and P K α 1 phases in Figure 2e–e-4, and the EDS line profiles also confirmed the uniform distributions of Co, Fe, B, and P after the thermal treatment in Figure 2f-1–f-4. Additional SEM images can be found in Figure S23, and the EDS spectra for the annealing temperature variation set and summary plot of atomic percentage are provided in Figure S24. There was no obvious elemental variation in the atomic percentage, indicating no dissociation and sublimation of elements.

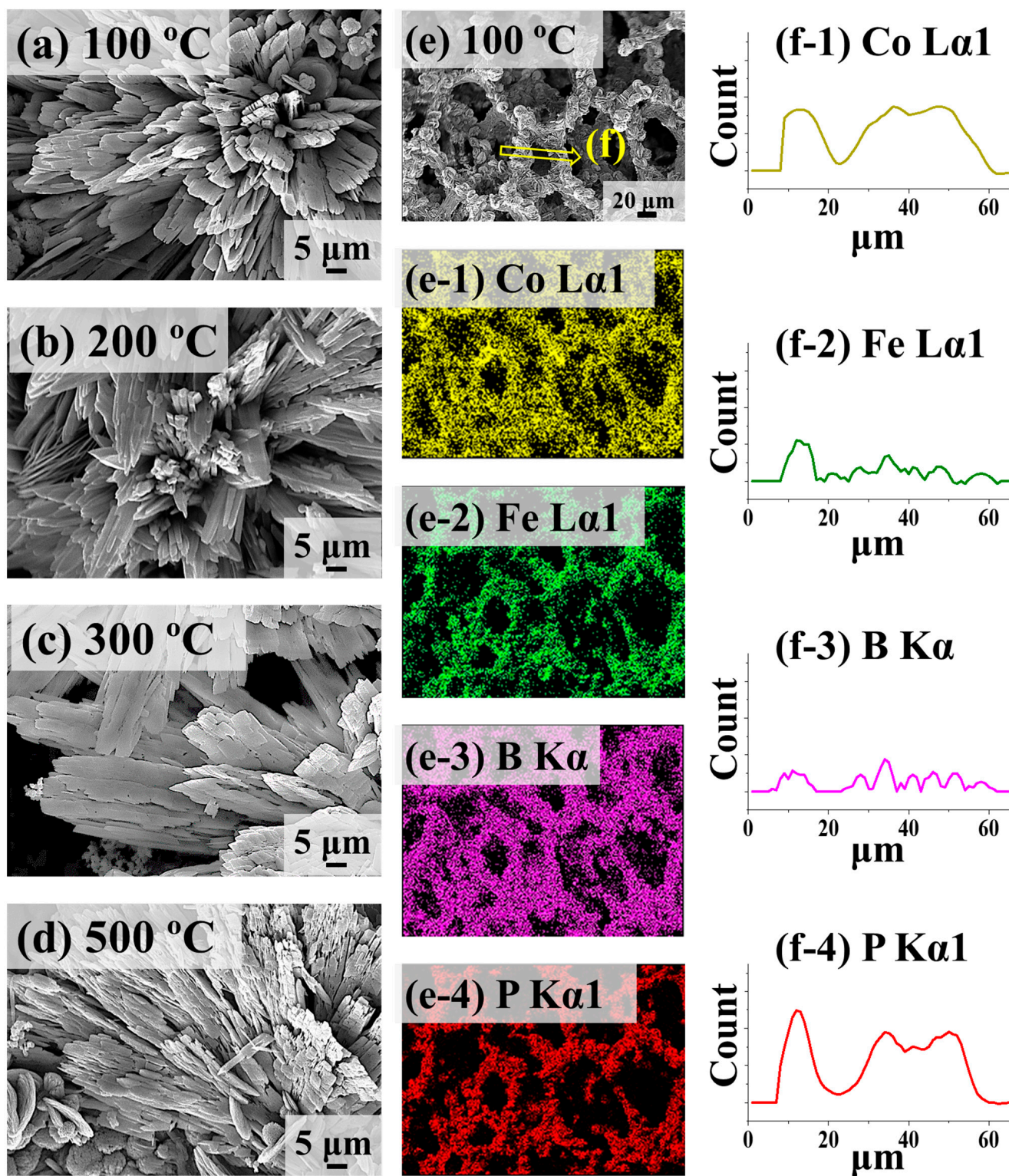


Figure 2. $\text{CoFeB}_{50}\text{P}_{50}$ micro-flower (MF) electrodes with annealing temperature variation. (a–d) SEM images of $\text{CoFeB}_{50}\text{P}_{50}$ MFs after annealing at different temperatures as labeled. (e–e-4) SEM image and corresponding EDS phase maps of 100 °C annealed sample. (f-1–f-4) EDS elemental line profiles from the location as indicated in (e).

Raman analysis was conducted to probe the crystal quality along with annealing, as seen in Figure 3a. The 100 °C annealing demonstrated the strongest Raman bands with Raman peaks at 261, 360, 478, 596, and 962 cm^{-1} , indicating the best crystal quality of CoFeBP MFs in this set [40]. The stretching vibration peaks at 950–1100 cm^{-1} may be associated with the oxygen bonds of metallic atoms (M-O-O) as indicated with the red dashed lines in Figure 3a [41,42]. At 100 °C, the peak split into two shoulder peaks, which could be related to the symmetric stretching O-O vibration [41,42]. More detailed Raman analysis can be found in the Supplementary Text S1.6. Figure 3b shows the XRD spectrum of the CoFeBP MF (100 °C) electrode. After annealing, the peak intensity was clearly intensified, suggesting improved local crystallinity [40]. Also, new XRD peaks appeared, i.e., at 22.8°, 60.8°, and 66.5°, again suggesting improved crystal quality with local lattice reconstruction due to the thermal-triggered adatom diffusion [38]. The multiple peaks clearly indicate a short-range polycrystal phase of CoFeBP MF, even after annealing [38]. The X-ray photoelectron spectroscopy (XPS) was conducted to probe the chemical states of Co, Fe, B, P, and O 1s and C 1s. The full-scan spectrum is shown in Figure 3c, and the zoom-in spectra are presented in Figure 3c-1–c-4. First, the O 1s and C 1s are due to surface oxidation and reference calibration. The O 1s spectrum in Figure S46a shows three distinct peaks located at 532.1, 539.9, and 534.5 eV, corresponding to M-O, M-OH, and absorbed H₂O, respectively (M=Co and Fe) [43]. The surface oxidation is inevitable due to air exposure, and C can always be observed along with reference calibration. In the Co 2p spectrum in Figure 3c-1, the binding energy (BE) of Co 2p_{1/2} and Co 2p_{3/2} was found at 793.6 and 778.5 eV, as compared with the pristine peak obtained in the XPS handbook (793.3 and 778.3 eV) [44], exhibiting positive shifts of 0.3 and 0.2 eV. The positive shift indicates the electron donation from Co atoms [45]. In the compound molecule formation, a positive shift of elemental electronic states indicates the donation of electrons in the ionic bonding. The peaks at 789.6 and 804.7 can be indexed to the satellite peaks [45]. The obtained dominant peaks along with their satellite peaks indicate the formation of Co₃O₄ on the surface [45,46]. The peaks centered at 795.9 and 780.8 eV indicate the existence of CoO on the surface [45,46]. In the Fe 2p spectrum in Figure 3c-2, the peaks located at 707.3 and 720.9 eV can be assigned to Fe⁰ (Fe 2p_{3/2} and Fe 2p_{1/2}). Similarly, positive shifts of 0.8 eV and 0.3 eV were observed, as compared with their pristine 720.1 and 707.0 eV, indicating electronic interaction with the non-metallic atoms [47]. The existence of 708.6 and 723.6 eV peaks represents the FeOOH, and the BEs at 712.3 and 727.2 eV can indicate the formation of Fe₃O₄ [48]. The peaks centered at 715.1 and 731.8 eV can be assigned to the shakeup satellite peak [49,50]. On the other hand, the B 1s level was negatively shifted by 2.4 eV (from 189.4 to 187.0 eV), indicating ionic bonding by electron acceptance. The 192.5 eV peak can be assigned to the B₂O₃ oxidation states [51]. In the P 2p spectrum, two dominant peaks appeared at 128.7 and 129.5 eV, which are assigned to P 2P_{3/2} and P 2P_{1/2}, respectively. The BEs of P 2P_{3/2} and P 2P_{1/2} were also negatively shifted to lower BE from the standard 129.9 to 128.7 eV and from 130.74 to 129.5 eV, implying electron acceptance to the p-orbital [52]. The strong electronegativity and electron affinity of P atoms can be beneficial for the strong bond formation [52]. The 133.4 eV peak belongs to the oxidized P species (P-O) [52]. Overall, the positive and negative shifts of elemental electronic states can imply strong ionic bonding, and oxidized states were found alongside them. More detailed XPS analysis can be seen in the Supplementary Text S1.10. In summary, from the structural analysis, the obtained structure should be a cobalt–iron–boron–phosphide (CoFeBP) alloy in the polycrystalline phase based on the XRD, XPS, and Raman analyses.

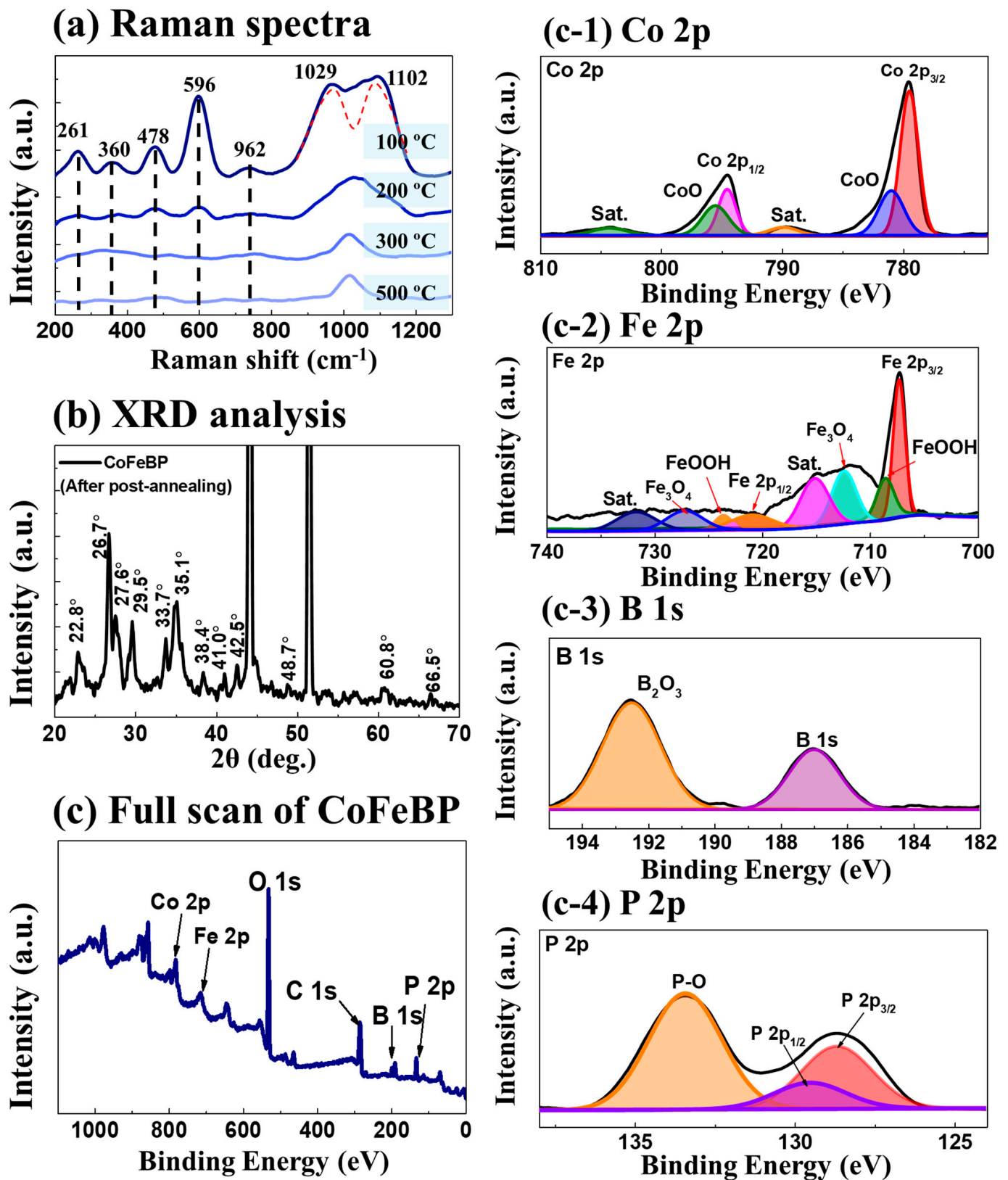


Figure 3. Surface characterizations for the best CoFeBP electrode annealed at 100 °C. (a) Raman spectra. (b) XRD spectrum. (c–c-4) XPS spectra of 100 °C CoFeB₅₀P₅₀ MF.

3. Electrochemical Analysis

3.1. The 3-E Electrochemical Properties of CoFeBP MFs

Figure 4 shows the 3-electrode (3-E) electrochemical characterizations of the post-annealing temperature variation set in 1 M KOH. The HER/OER LSV results are shown in Figure 4a–b, where the 100 °C CoFeBP MF exhibited the best catalytic performances with the lowest overpotential values of 145 and 424 mV at 200 mA/cm², as summarized in Figure 4c. Figure 4d,e show the HER/OER Tafel slope values, derived based on the relation [53] $\eta = a + b \log | -j |$, where η presents the overpotential, a is the Tafel constant, and b represents the Tafel slope. The 100 °C CoFeBP MFs showed the lowest HER/OER Tafel values of 62.0 and 199 mV/dec, as seen in Figure 4f, indicating the best charge transfer kinetics and reaction speed in this set [54]. While the HER Tafel value was quite good, the OER Tafel value was relatively high, which can negatively affect the catalytic performance in bifunctional 2-E performance. HER/OER Nyquist plots by the electrochemical impedance spectroscopy (EIS) are shown in Figure 4g,h, which can provide insights into the impedance of electrochemical systems, such as the solution resistance (R_s) and charge transfer resistance (R_{ct}) [55]. Further, 100 °C CoFeBP MFs exhibited the lowest HER/OER charge transfer resistance (R_{ct}) values of 7.1 and 13.3 Ω , suggesting the highest HER/OER charge transport characteristics in this set [56,57]. The HER/OER double-layer capacitance (C_{dl}) is summarized in Figure 4i, which was derived from the CV plots via the following relation, $J = (J_a - J_c)/2$, where J_a is the anodic current and J_c is the cathode current [57]. The corresponding CV plots are provided in Figures S26–S28. The 100 °C MFs demonstrated the highest HER/OER C_{dl} values of 4.6 and 14.5 mF/cm², suggesting the largest electrochemical surface area (ECSA) of 100 °C CoFeBP MFs. The C_{dl} values are specifically related to the capacitance at the electrode–electrolyte interface and, generally, the OER C_{dl} values are higher. The HER is a 2-electron transfer process, and OER is a 4-electron transfer process. Thus, the OER requires higher voltages. This can indicate that more metallic sites participate in the OER process. With a higher voltage application, we can observe larger current changes, which are reflected as higher C_{dl} values. The 3-E electrochemical properties of the best CoFeBP MF in 1 M KOH are summarized in Table 1.

The HER operation can be summarized: Volmer step: $H_2O + e^- + M \rightarrow OH^- + MH_{ad}$; Heyrovsky step: $H_2O + e^- + MH_{ad} \rightarrow M + OH^- + H_2$; or Tafel reaction: $2MH_{ad} \rightarrow 2M + H_2$ [58]. The M is the metallic site (Co and Fe), and H_{ad} is the adsorbed hydrogen proton. The OER process can be summarized: $OH^- + M = M-OH + e^-$, $M-OH + OH^- = M-O + H_2O + e^-$, $2M-O \rightarrow 2M + O_2$. Alternatively, $M-O + OH^- = M-OOH + e^-$; $M-OOH + OH^- \rightarrow O_2 + H_2O + e^- + M$ [40,58]. It is important to have a lower energy barrier to break the covalent H-O-H bonds. The efficient H_{ad} and hydroxyl adsorption/release steps are imperative for the efficient HER/OER processes in alkaline solutions. The multi-metallic active centers in the CoFeBP MFs can effectively break the tetrahedral covalent H_2O bond and form the metal hydride and hydroxyl intermediates (MH_{ad} and $M-OOH$), allowing for continuous hydrogen and oxygen generation via the HER and OER steps [59,60]. The micro-flower morphology can provide a largely increased number of absorption sites, in which the MH_{ad} and $M-OOH$ intermediates can easily be increased [60]. The incorporation of B atoms can result in the modulation of electronic states for active sites, leading to efficient catalytic reactions and higher electronic conductivity for higher HER/OER rates [61,62]. At the same time, P is a well-known element for superior HER/OER activities with its strong electronegativity, and the inclusion of P can significantly improve the HER/OER kinetics and performances in the MF matrix [62].

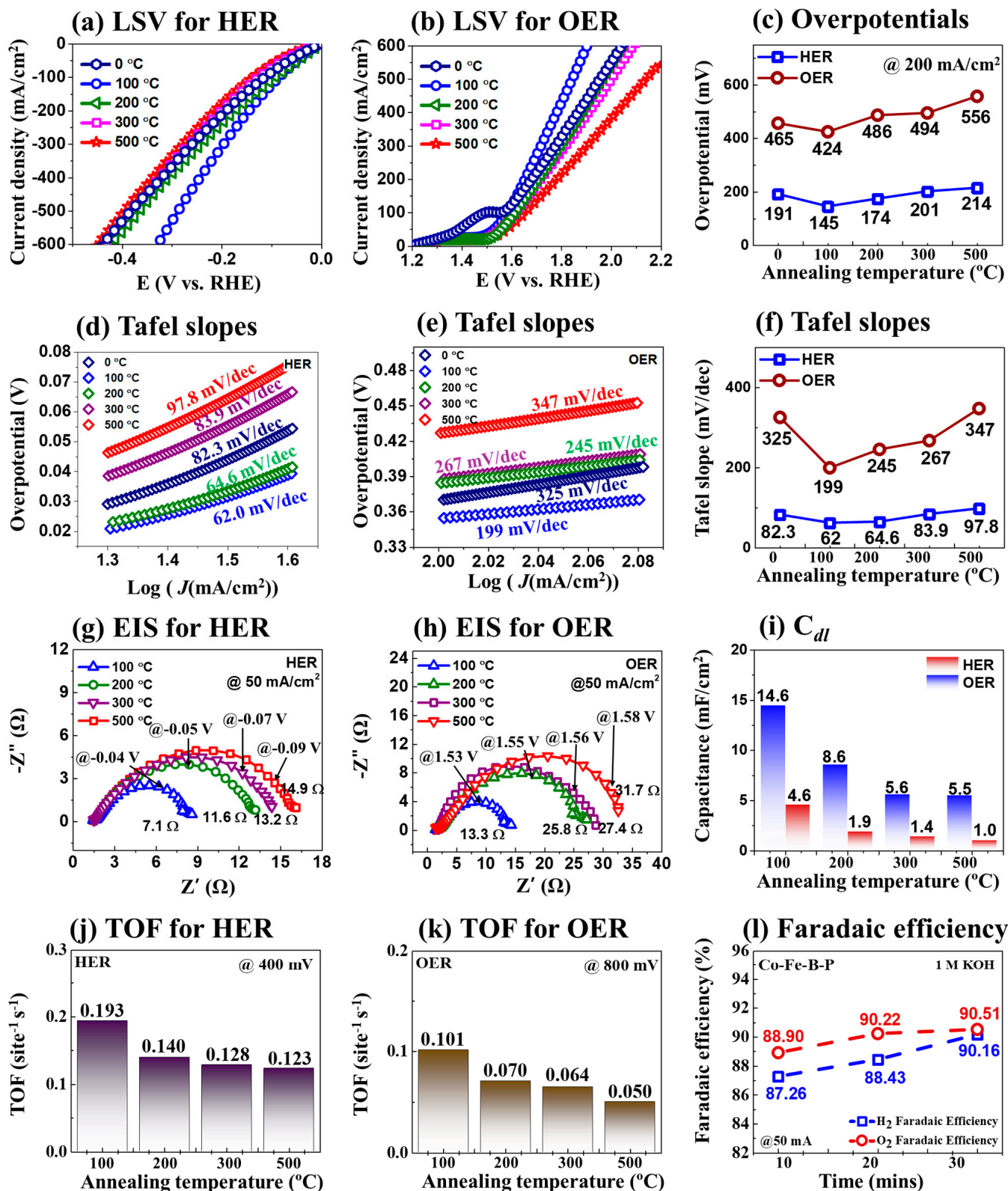


Figure 4. The 3-E electrochemical characterizations of the CoFeB₅₀P₅₀ MF electrodes in 1 M KOH. (a,b) HER and OER LSV curves in the post-annealing temperature variation set. (c) HER and OER LSV value summary at 200 mA/cm². (d,e) HER and OER Tafel slope plots. (f) Corresponding Tafel slope values. (g,h) EIS plots. (i) Double-layer capacitance (C_{dl}) obtained from the corresponding CV curves. (j,k) HER and OER turnover frequency (TOF) plots. (l) HER and OER Faradaic efficiency (FE).

Table 1. Summary of 3-E HER/OER electrochemical properties of the best CoFeBP electrode in 1 M KOH solution.

Electrochemical Properties	HER	OER
EIS values	7.1 Ω	13.3 Ω
Tafel slopes	62 mV/dec	199 mV/dec
C_{dl} values	4.6 mF/cm ²	14.6 mF/cm ²
ECSA	28.75 cm ²	91.25 cm ²
TOF values (at 500 and 800 mA/cm ²)	0.193 site ⁻¹ s ⁻¹	0.101 site ⁻¹ s ⁻¹
Faradic efficiency (FE)	90.51%	90.16%

The turnover frequency (TOF) of CoFeBP MFs is calculated as seen in Figure 4j,k. The TOF can be utilized to reflect the intrinsic activity of electrodes along with the number of H₂ and O₂ molecules generated per site and time at the turnover [63]. The 100 °C electrode yields the highest HER/OER TOF values of 0.193 and 0.101 site⁻¹s⁻¹, as summarized in Figure 4j,k. The comparison of HER/OER TOF values with other electrocatalysts is summarized in Table S1. The HER and OER Faradaic efficiency was calculated to assess the energy efficiency in Figure 4l [64]. The generated H₂ or O₂ was collected by the water displacement approach, as seen in Figure S36. The HER/OER Faradaic efficiency of optimized CoFeBP MFs was found to have relatively high efficiencies of 90.16% and 90.20% for 30 min, as summarized in Figure 4l [14]. The efficiency loss could be due to the heat generation and bubble formation [65]. More details on the TOF and Faradaic efficiency calculations can be found in the Supplementary Text S1.8 and S1.9.

In addition, the formation of oxidation peaks was observed in the OER LSV curves, as seen in Figure 4b. The oxidation peak gradually increased along with the increased performance of samples, and a higher oxidation current was observed with a better-performing sample. To observe the oxidation and reduction peak formation in the same range of OER, cyclic voltammetry (CV) was performed, as seen in Figure S35. The oxidation state was observed at ~1.48 V, which can be due to the formation of M-OOH (Co and Fe), i.e., cobalt hydroxide (CoOOH), cobalt oxide (Co₃O₄), iron hydroxide (Fe-OOH), and other Fe-oxide species [66]. During the positive scan, the formation of a 1.48 V peak can be due to the formation of M-OOH, i.e., (M(OH)₂ + OH⁻ → MOOH + H₂O + e⁻; 3M(OH)₂ + 2OH⁻ → M₃O₄ + 4H₂O + 2e⁻) [67,68]. In the process of a negative scan, reversible reactions can take place with the reduction peak at ~1.39 V, and the Fe⁻ and Co-oxide species can be reduced to M(OH)₂. The Fe/Co oxide peak formation can improve the OER performance as the M-OOH (Co, Fe) can directly take part in the OER process as an OER intermediate and can function as active OER centers, further boosting the splitting process [67,68].

Overall, the 100 °C CoFeBP MFs demonstrated the best electrochemical activities in this set, which are mainly due to the improved crystallinity and effectively boosted carrier transport in moderate annealing conditions [69]. Specifically, during the vacuum annealing process, hydroxyl groups can be eliminated, and the oxygen vacancies (O_{vac}) can be removed [54,70]. The defect density can be altered by atomic diffusion, and thermal treatment is crucial in the modulation of surface active sites [40]. Nevertheless, excessive thermal energy can damage MF structures, indicating limited performance [40]. XRD, Raman, EIS, and LSV analyses before/after annealing on CoFeBP MFs can be found in the Supplementary Text S1.6., S1.7. and S1.11 in Figures S29–S32.

3.2. The 3-E LSV Activity of CoFeBP MFs in Different pH Media

Figure 5 shows the 3-E HER/OER performances of the best CoFeBP MF in different pH electrolytes, as compared with the Pt/C and RuO₂ benchmark electrodes. The alkaline, acidic and neutral media were prepared as 1.0 M KOH, 0.5 M H₂SO₄, and 1.0 M PBS solutions. The reference electrode fabrication of Pt/C and RuO₂ can be found in the Supplementary Text S1.4 along with Figures S4 and S5. As seen in Figure 5a–f, the 3-E HER/OER performances were the best in alkaline conditions and worst in the neutral

medium in the order of 1 M KOH > 0.5 M H₂SO₄ > 1 M PBS. The reference electrodes of Pt/C and RuO₂ demonstrated better HER/OER performances in all electrolytes due to the excellent inherent electrocatalytic properties of reference electrodes. Meanwhile, the CoFeBP MFs demonstrated quite comparable HER/OER performances in the alkaline media in Figure 5a,d: 196 and 130 mV for HER and 397 and 491 mV at 300 mA/cm². The lower performance in the acidic media could be due to the high concentrations of H⁺ ions, and, generally, performance degradation and corrosion of transition metal-based electrodes can be observed in acidic solutions [71]. The neutral media showed the worst performance due to the lack of conductive ions [40]. The 3-E steady-state measurements in alkaline media (1.0 M KOH) were carried out further to understand the stability of CoFeBP MFs at various overpotentials (Figure 5g). The CA measurement checks the initial fluctuation and compares the result to LSV. The 3-E CA response demonstrated a negligible difference with LSV, as summarized in Figure S38, confirming the excellent early-stage stable operation of CoFeBP MFs. The HER/OER performance of CoFeBP MFs is compared with the state-of-the-art transition metal-based electrodes at 20 mA/cm² in Figure 5h,i and Tables 2 and 3. The CoFeBP MF demonstrated an excellent HER performance of 20 mV at 20 mA/cm², which ranked it as the second-best HER electrode as compared with the state of the art in Figure 5h and Table 2. At the same time, CoFeBP MF demonstrated a decent OER performance of 219 mV at 20 mA/cm², which ranked it as the sixth-best transition metal-based OER electrode (Figure 5i and Table 3). However, the OER performance was not as high as HER.

Table 2. The 3-E hydrogen evolution reaction (HER) electrocatalytic performance comparison with various transition metal-based catalysts in 1.0 M KOH.

Electrocatalyst	Overpotentials [mV]			Year	References
	@20 mA/cm ²	@50 mA/cm ²	@200 mA/cm ²		
RuVNi	15	26	48	2019	[72]
CoFeBP	20.1	46	145	-	This work
NiMoB	54	97	210	2022	[40]
Ru/CoFeP	61	82	-	2020	[19]
NiFeMn	80	121	-	2020	[73]
CoB@CoO/Ti	81	110	181	2017	[74]
NiCoP	134	165	204	2018	[13]
Ni/Ni ₃ N	151	232	420	2015	[59]
Fe-NiSe	182	265	-	2022	[75]
Fe-S	193	235	324	2019	[76]

Table 3. The 3-E oxygen evolution reaction (OER) electrocatalytic performance comparison with various transition metal-based catalysts in 1.0 M KOH.

Electrocatalyst	Overpotentials [mV]			Year	References
	@20 mA/cm ²	@50 mA/cm ²	@200 mA/cm ²		
Ni ₂ P-CuP	140	190	-	2021	[3]
MoNiP _x /NiS _y	143	156	221	2021	[77]
NiMo ₃ S ₄	162	252	617	2022	[78]
P-Co ₃ O ₄	208	295	330	2018	[18]
RuVNi	217	227	312	2019	[72]
CoFeBP	219	303	426	-	This work
NiMoB	248	267	500	2022	[40]
NiFeMn	260	291	352	2020	[73]
NiCoP	296	328	370	2018	[13]
Mo ₂ NiB ₂	311	342	-	2021	[2]
NiSe ₂	320	521	-	2022	[75]

alkaline media and higher operational temperature due to the better water-splitting (WS) performance [64,79]. Further, 100 h stability operation was carried out in the industrial operational conditions in 6 M KOH at 60 °C in Figure 6e. The 100 h stability operation of 2-E CoFeBP||CoFeBP MFs clearly confirmed the superior stability of CoFeBP MFs with the very stable current, with only a minor current fluctuation at 1000 mA/cm² in the industrial operational conditions. There was no significant dissolution of CoFeBP MFs under the industrial operational condition. After the continuous 100 h operation, small particles were observed at the bottom of the cell. The CoFeBP MFs demonstrated excellent repeatability, with minor differences after 1000 cycles in Figure 6f, further confirming the excellent stability of CoFeBP MFs. In addition, the 12 h stability tests in 1 and 6 M KOH at 1000 mA/cm² at room temperature also confirmed excellent stability, as seen in Figure S40.

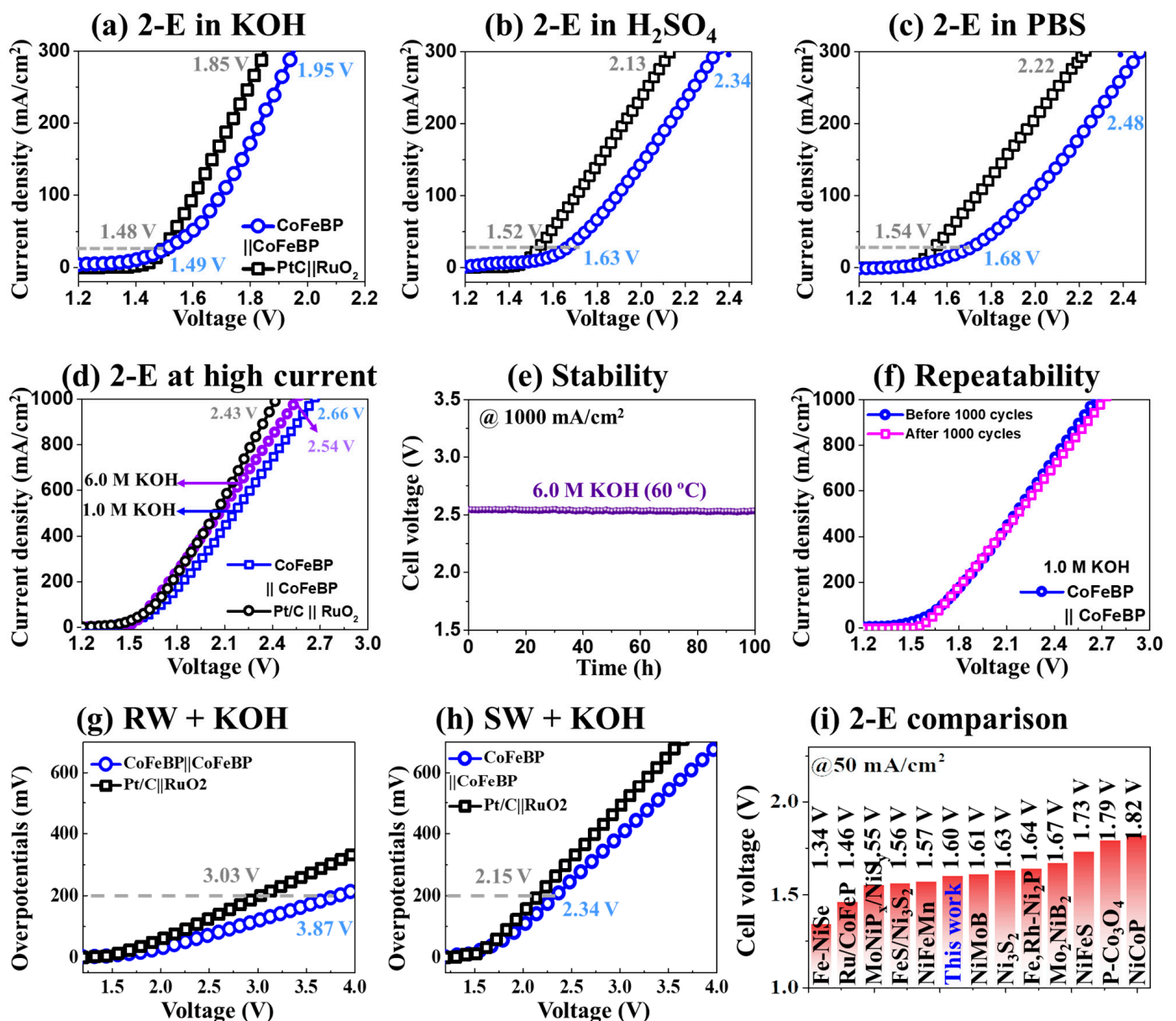


Figure 6. (a–c) 2-E activity in different media. (d) LSV up to 1000 mA/cm². (e) Stability test in 6.0 M KOH at 60 °C for 100 h. (f) 2-E repeatability in 1.0 M KOH after 1000 cycles. (g) 2-E catalytic performance in natural seawater (SW) and river water (RW). (h) 2-E performance in SW with the addition of 1 M KOH. (i) 2-E performance comparison with the state-of-the-art electrodes at 50 mA/cm².

The water splitting (WS) of CoFeBP MFs in natural seawater (SW) and river water (RW) with the addition of 1.0 M KOH was performed, as seen in Figure 6g,h. Bare SW and RW performances can be seen in Figure S41. Generally, CoFeBP MFs demonstrated higher WS performances in SW over RW. The 1.0 M KOH addition largely improved the WS performance due to the boosted solution conductivity by the increased OH⁻ ions. The 2-E cell voltages of 3.87 and 2.34 V in RW and SW were obtained at 200 mA/cm² by the CoFeBP MFs, as seen in Figure 6g,h. The higher WS performance in SW can be due to the presence of conductive ions, such as Na⁺ and Cl⁻ [40]. In natural waters, a lot of ions and biological compounds and elements, such as Mg⁺, F⁻, Ca⁺, Br⁻, bacteria, and dust particles exist, and, thus, the WS performance in natural waters is generally much worse than DI water-based solutions [40]. The CA response in SW + 1.0 M KOH was measured, as seen in Figure S42. Stable current output was obtained in 30 min continuous operations at various voltages, which confirmed the stable operation of CoFeBP MFs in natural waters. Overall, the CoFeBP MF showed WS performance and stability in real waters. The 2-E cell voltages in various electrolytes and natural waters are summarized in Table 4. Finally, the CoFeBP MF demonstrated an outstanding 2-E cell voltage of 1.60 V at 50 mA/cm², and CoFeBP MF may be one of the best transition metal-based electrocatalysts, as compared with the state of the art, as summarized in Figure 6i and Table 5.

Table 4. The 2-E (CoFeBP||CoFeBP) cell voltage summary of LSV performance of the best CoFeBP electrode in different electrolytes.

Electrolytes	@200 mA/cm ²	@1000 mA/cm ²
1 M KOH	1.84 V	2.66 V
6 M KOH	1.76 V	2.54 V
0.5 M H ₂ SO ₄	2.13 V	-
1 M PBS	2.25 V	-
River water	-	-
River water + 1 M KOH	3.87 V	-
Seawater	-	-
Seawater + 1 M KOH	2.34 V	-

Table 5. The 2-E electrocatalytic performance comparison of overall water splitting with various transition metal-based catalysts in 1.0 M KOH.

Electrocatalyst	Electrolyte	Cell Voltage (V)		Year	References
		@50 mA/cm ²	@200 mA/cm ²		
Fe-NiSe	1 M KOH	1.34 V	1.61 V	2022	[75]
Ru/CoFeP	1 M KOH	1.46 V	-	2020	[19]
MoNiP _x /NiS _y	1 M KOH	1.55 V	1.88 V	2021	[77]
FeS/Ni ₃ S ₂	1 M KOH	1.56 V	-	2022	[80]
NiFeMn	1 M KOH	1.57 V	1.66 V	2020	[73]
CoFeBP	1 M KOH	1.60 V	1.84 V	-	This work
NiMoB	1 M KOH	1.61 V	1.96 V	2022	[40]
Ni ₃ S ₂	1 M KOH	1.63 V	-	2018	[81]
Fe,Rh-Ni ₂ P	1 M KOH	1.64 V	1.85 V	2022	[82]
Mo ₂ NiB ₂	1 M KOH	1.67 V	-	2021	[2]
NiFeS	1 M KOH	1.73 V	-	2022	[83]
P-Co ₃ O ₄	1 M KOH	1.79 V	-	2018	[18]
NiCoP	1 M KOH	1.82 V	-	2018	[13]

3.4. Characterization after Stability Test

The CoFeBP MFs (anode) are characterized before/after 12 h stability operation in 1 M KOH at 1000 mA/cm² in Figure 7. Anode data are shown here as more obvious changes can be generally observed on the anode side. Additional data can be seen in Figures S43–S45. Firstly, the SEM images showed no visible difference before/after the long

stability operation in Figure 7a,a-1. Upon closer viewing, the edges of branches became slightly rougher after the 12 h stability operation; however, the micro-flower structures were well maintained. This indicates the good structural stability of CoFeBP MFs. The SEM images of the cathode and anode after the 12 h stability operation are shown in Figure S43. There was also no obvious difference observed in either electrode. The Raman spectrum of the CoFeBP MF anode after stability testing is shown in Figure 7b. Raman bands of the anode and cathode after the 12 h stability test are compared in Figure S44. The Raman of CoFeBP MF before the stability test can be seen in Figure 3a. In general, the Raman intensity was largely reduced after the 12 h stability test. The Raman intensity reduction could be due to the formation of oxide species after the long-term stability operations at high current [41,42]. The 360 and 962 cm^{-1} peaks disappeared, and this may be due to the originally weak Raman band signals being blocked by the various oxide formations. The anode showed a greater reduction, as clearly seen in Figure S44.

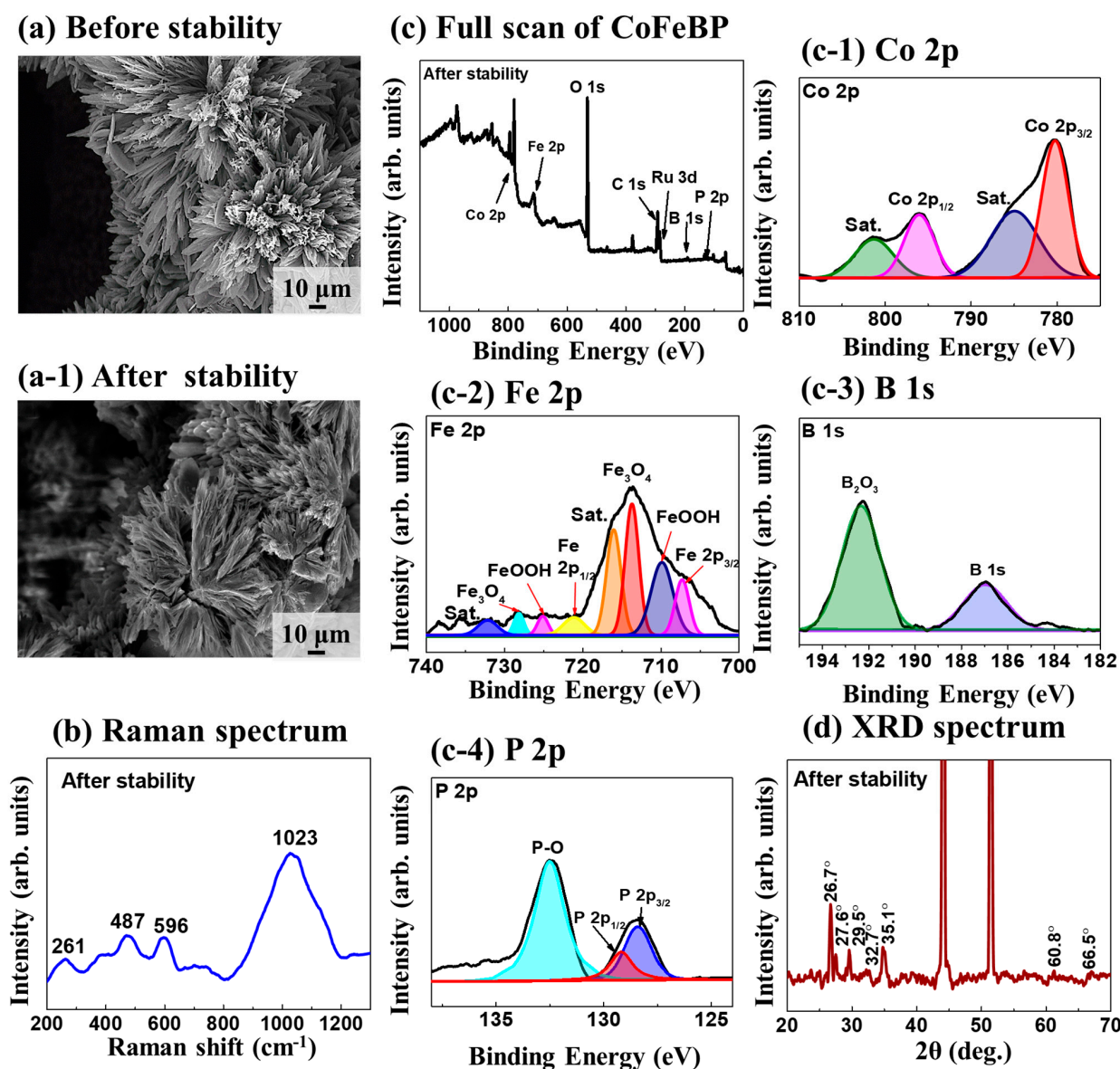


Figure 7. Characterizations of CoFeBP MF after the stability for 12 h at 1000 mA/cm^2 . **(a,a-1)** SEM images of CoFeBP (anode) before and after stability test. **(b)** Raman spectrum of anode after stability test. **(c-c-4)** XPS spectra of Co 2p, Fe 2p, B 1s and P 2p. **(d)** XRD pattern of anode after stability test.

The XPS spectra of the anode after the stability test are shown in Figure 7c–c-3. In the Co 2p spectrum in Figure 7c-1, the Co 2p_{3/2} and 2p_{1/2} peaks are found at 780.2 and 795.9 eV, and the corresponding satellite peaks are centered at 784.8 and 801.2 eV, indicating the existence of Co(OH)₂ on the electrode surface after stability tests. The oxide-related peaks were largely increased, as clearly seen in Figure 7c-1. This may be due to the continuous redox reactions in OH[−]-containing solution [84]. In the Fe spectrum, similarly, the proportion of oxidized Fe species was also largely increased and taller than the Fe 2P peaks, as seen in Figure 7c-2. In the B 1s and P 2p spectra, increased B and P oxidation peaks were similarly observed, as seen in Figure 7c-3,c-4, resulting from the intense oxidation during the water-splitting process. For the O 1s spectrum, as seen in Figure S46b, the increased portion of M-O bonds further confirmed the formation of oxidation states [85]. The XRD pattern after the stability test is provided in Figure 7d, which can be compared with that in Figure 3b before the stability test. Generally, the intensity of XRD diffraction peaks was reduced, and many diffraction peaks disappeared. For example, the diffraction peaks at 22.8, 33.7, 38.4, 41.0, and 42.5° were not visible after the stability test due to the reconstruction of the surface by the formation of an amorphous oxide layer during the water-splitting operation [37]. The peak intensity at 26.7, 27.6, 29.5, and 35.1° decreased, again indicating the formation of an amorphous oxide layer. The oxidation of CoFeBP MF surfaces can generally occur in the initial stages of WS operations, as discussed previously, with the oxidation peak formation, and it stabilizes after multiple operations. Indeed, surface oxidation improves the OER performance as the oxidated species can act as OER active sites in the catalytic process [37,86]. The LSV performance of the CoFeBP electrode after stability testing was examined in 1.0 M KOH, as seen in Figure S45, and only minor differences were observed.

4. Conclusions

In summary, a CoFeBP micro flower (MF) was successfully fabricated via hydrothermal synthesis, and the reaction parameters were systematically optimized. The best optimized CoFeBP MF electrode demonstrated comparable 3-E and 2-E performances with the benchmarks of Pt/C and RuO₂. Specifically, the CoFeBP MF demonstrated an HER overpotential of 20.1 mV at 20 mA/cm² in 1.0 M KOH. The OER overpotential value of the CoFeBP MF electrode was 219 mV at 20 mA/cm² in 1.0 M KOH. While the HER performance was relatively strong, the OER performance indicated room for further improvement. The bifunctional CoFeBP MFs exhibited a cell voltage of 1.60 V at 50 mA/cm² in 1.0 M KOH. The 2-E performance was quite good; it still showed some room for further improvement, as compared with the state-of-the-art electrocatalysts. In addition, the CoFeBP MFs demonstrated excellent durability, stability, and repeatability at high current and high temperatures in high-alkaline solutions. The CoFeBP MFs demonstrated excellent performances in natural seawater and seawater + KOH solutions. The surface oxidation was systematically characterized after the 12 h stability operation at 1000 mA/cm². The improved performance of CoFeBP MFs can also be attributed to the high ECSA by the distinctive micro-flower morphology and improved short-range local crystallinity by the systematic annealing optimization. Synergy between the elements was effectively utilized, i.e., highly active intrinsic properties by electron-enriched Co and Fe active sites with the incorporation of B and P.

Supplementary Materials: The following supporting information can be downloaded at: <https://www.mdpi.com/article/10.3390/nano14080698/s1>, Figure S1: (a–a-1) Scanning electron microscope (SEM) images of porous nickel foam (NF). (b–b-2) SEM image and corresponding EDS phase maps of porous NF. (c) EDS spectrum with the atomic percentage. (d,e) hydrogen evolution reaction (HER) and oxygen evolution reaction (OER) activities of porous NF in 1 M KOH. More details on the preparation of substrate and precursors can be found in the Supplementary Text S1.1. Figure S2: (a,b) hydrogen evolution reaction (HER) and oxygen evolution reaction (OER) activities of the best CoFeBP MF at different scan rates between approximately 2 and 10 mV/s. (a-1,b-1) Corresponding Tafel slopes; 5 mV/s demonstrated the optimized scan rate and, thus, it was adapted for further

LSV measurements. More details can be found in the Supplementary Text S1.2. Figure S3: Electrochemical impedance spectroscopy (EIS) measurements for the optimized CoFeBP MF electrode at different voltages. (a) HER EIS. (b) OER EIS. Voltage variation at fixed current was adapted for further EIS measurements. More details can be found in the Supplementary Text S1.2. Figure S4: (a,a-1) SEM images of Pt/C reference electrode. (b) EDS spectrum. (c,c-1) HER activity of Pt/C electrode and corresponding overpotential values at different current densities. More details can be found in the Supplementary Text S1.4. Figure S5: (a,a-1) SEM images of RuO₂ reference electrode. (b) EDS spectrum. (c,c-1) OER activity of RuO₂ electrode and corresponding overpotential values at different current densities. More details can be found in the Supplementary Text S1.4. Figure S6: Fabrication steps of CoFeBP micro flower (MF) electrode on the porous nickel foam (NF) via the hydrothermal reaction. The best sample from the hydrothermal reaction was treated with post-annealing. More details on the fabrication of CoFeBP MF can be found in the Supplementary Text S1.5. Figure S7: (a–d) SEM images of CoFeBP electrodes at different reaction duration. (a-1–a-3,b-1–b-3,c-1–c-3,d-1–d-3) Corresponding zoom-in images. Figure S8: HER/OER performances of CoFeBP electrodes with hydrothermal deposition time variation. (a,b) HER/OER LSV results. (a-1,b-1) Corresponding overpotential values at 200 mA/cm². (a-2,b-2) HER/OER overpotential values of the best electrode at 200 mA/cm². Figure S9: (a–d) SEM images of CoFeBP electrodes with hydrothermal reaction temperature variation. (a-1–a-3,b-1–b-3,c-1–c-3,d-1–d-3) Corresponding zoom-in images. Figure S10: HER/OER performances of CoFeBP electrodes with hydrothermal reaction temperature variation. The duration of hydrothermal process was fixed for 8 h. (a,b) HER/OER LSV results. (a-1,b-1) Corresponding overpotential values at 200 mA/cm². (a-2,b-2) HER/OER overpotential values of the best electrode at 200 mA/cm². Figure S11: (a–g) SEM images of CoFeBP MF electrodes with the B-P concentration variation. (a-1–g-1) Corresponding zoom-in images. Figure S12: (a–g) EDS spectra of CoFeBP electrodes in the B-P concentration variation. (h) Summary plot of atomic percentage. Figure S13: (a,b) HER/OER LSV summary of B-P concentration variation set. (a-1,b-1) Corresponding overpotential values at 200 mA/cm². (a-2,b-2) HER/OER overpotential values of the best electrode at 200 mA/cm². Figure S14: (a–f) SEM images of CoFeBP MF electrodes with the Co-Fe concentration variation. (a-1–f-1) Corresponding zoom-in images. Figure S15: (a–f) EDS spectra of CoFeBP electrodes in the Co-Fe concentration variation. (g) Atomic percentage summary plot. Figure S16: (a,b) HER/OER LSV results. (a-1,b-1) Corresponding overpotential values at 200 mA/cm². (a-2,b-2) HER/OER overpotential values of the best electrode at 200 mA/cm². Figure S17: (a–d) SEM images of CoFeBP electrodes at different urea concentration. (a-1–a-3,b-1–b-3,c-1–c-3,d-1–d-3) Corresponding zoom-in images. Different urea concentration resulted in altered morphologies of CoFeBP. Figure S18: HER/OER performances of CoFeBP electrodes with urea concentration variation. Hydrothermal reaction parameter was fixed at 4 h at 140 °C. (a,b) HER/OER LSV results. (a-1,b-1) Corresponding overpotential values at 200 mA/cm². (a-2,b-2) HER/OER overpotential values of the best electrode at 200 mA/cm². Figure S19: (a–f) SEM images of Urea-Ammonium fluoride concentration variation. (a-1–f-1) Corresponding zoom-in images. Figure S20: Electrochemical performance of CoFeBP electrodes with Urea-Ammonium fluoride concentration variation set. (a,b) HER/OER LSV results. (a-1,b-1) Corresponding overpotential values at 200 mA/cm². (a-2,b-2) HER/OER overpotential values of the best electrode at 200 mA/cm². Figure S21: (a–d) SEM images of CoFeBP electrodes with post-annealing duration variation. The Annealing temperature was fixed at 100 °C. (a-1–d-1) Corresponding zoom-in images. Figure S22: HER/OER performance of CoFeBP electrodes with post-annealing time variation. (a,b) HER/OER LSV results. (a-1,b-1) Corresponding overpotential values at 200 mA/cm². (a-2,b-2) HER/OER overpotential values of the best electrode at 200 mA/cm². Figure S23: (a–d) SEM images of hybrid CoFeBP electrodes with post-annealing temperature variation. Annealing duration was fixed at 30 min. (a-1–d-1) Corresponding zoom-in images. Figure S24: (a–d) EDS spectra of post-annealing temperature variation set. (e) Summary plot of atomic percentage changes. Generally, they showed similar atomic percentage with minor changes with post-annealing temperature variation. Figure S25: HER/OER performance of CoFeBP electrodes with post-annealing time variation. (a,b) HER/OER LSV results. (a-1,b-1) Corresponding overpotential values at 200 mA/cm². (a-2,b-2) HER/OER overpotential values of the best electrode at 200 mA/cm². Figure S26: (a–d) HER CV curves of CoFeBP electrodes in the post-annealing temperature variation set. The scan rate changes from 40 mV/s to 180 mW/s. More details can be found in S-1.2. Figure S27: (a–d) OER CV curves of CoFeBP electrodes in the post-annealing temperature variation set. The scan rate changes from 40 mV/s to 180 mW/s. More details can be found in S-1.2. Figure S28: (a,b) HER/OER anodic and

cathodic current density as a function of scan rate. (a-1,b-1) HER/OER C_{dl} plots. More details can be found in S-1.2. Figure S29: (a) Raman analysis of the best CoFeBP electrodes before and after post-annealing. More details can be found in S-1.6. Figure S30: (a,b) XRD analysis of the best CoFeBP electrodes before and after post-annealing. (a-1,a-2,b-1,b-2) Corresponding zoom-in spectra. More details can be found in S-1.7. Figure S31: (a,b) HER/OER EIS of the best CoFeBP electrodes before and after post-annealing. Figure S32: (a,b) HER and OER LSV activities of the best CoFeBP electrodes before and after post-annealing. Figure S33: (a–d) XRD spectra of CoFeBP, CoFeP, CoBP and CoFeB electrodes. Figure S34: (a–d) Related PDF cards. (http://icsd.kisti.re.kr/icsd/icsd_chemistry.jsp) accessed on 1 June 2020, Figure S35: (a) Cyclic voltammetry (CV) measurement of $Co_{90}Fe_{10}B_{50}P_{50}$ MF electrode in the same scanning range as OER. (a-1) Zoom-in plot of oxidation and reduction peaks. Figure S36: (a) Water-gas displacement to collect the generated H_2 and O_2 by 3-E HER/OER operations. More details can be found in S-1.9. Figure S37: (a,b) Comparison of theoretical values and measured H_2 and O_2 in different reaction time. More details can be found in S-1.9. Figure S38: (a,b) HER/OER 3-E current density comparisons of CA and LSV. (a-1,b-1) Difference in percentage. Figure S39: (a) CA response of the best CoFeBP MFs in 1 M KOH. (b) Comparison of 2-E current density of CA and LSV. Figure S40: (a) 2-E stability test of CoFeBP | CoFeBP MFs. The 1.0 M KOH stability was performed at room temperature at 1000 mA/cm^2 for 12 h. The 6.0 M KOH stability was performed at $60\text{ }^\circ\text{C}$ at 1000 mA/cm^2 for 12 h. Figure S41: (a) LSV results of CoFeBP | CoFeBP MFs in sea and river waters. While naggable water splitting (WS) was observed in river water (RW), higher WS was observed in the seawater (SW) by the CoFeBP MFs. General conductivity of RW is ~ 1 milli-siemens per centimeter (mS/cm) and it reaches ~ 50 mS/cm in SW. Notably, in SW, due to the existence of Cl^- ions, the chlorine evolution reaction (CER) is inevitable since the required energy for the formation of hypochlorite is comparable to OER, ($Cl^- + 2OH^- = ClO^- + H_2O + 2e^-$), which will compete with oxygen generation reaction and corrode the electrode [47]. The obtained results were comparable to the reference system, meaning that the MBF CoFeBP catalyst presented superior OER and chloride corrosion resistance, which can effectively suppress the CER. Figure S42: (a) CA response in seawater + 1 M KOH of the best CoFeBP electrode. (b) Comparison of the current density of LSV and CA. Figure S43: (a,b) SEM images of CoFeBP MFs after 2-E stability test at 1000 mA/cm^2 in 1.0 M KOH for 12 h. Figure S44: (a) Raman spectra of anode and cathode CoFeBP MFs after 12 h stability test. More details can be found in S1.6. Figure S45: (a,b) HER and OER activities of CoFeBP MFs after 12 h stability test. Figure S46: (a) XPS spectrum of O 1s. Table S1: TOF comparison of electrocatalysts for HER and OER. References [87–121] are cited in Supplementary Materials.

Author Contributions: S.L., M.A.H., M.H.J. and R.M. participated in the experiment design and carried out the experiments. S.L., M.A.H., M.H.J. and S.A.D. participated in the characterization and analysis of data. J.-H.J., Y.-U.C. and J.L. designed the experiments and testing methods. S.L., J.-H.J. and J.L. carried out the writing. All authors have read and agreed to the published version of the manuscript.

Funding: This research was supported by the Core Research Institute Basic Science Research Program through the National Research Foundation of Korea (NRF) funded by the Ministry of Education (No. 2018R1A6A1A03025242) and in part by a research grant from Kwangwoon University in 2024.

Data Availability Statement: Data will be available upon request.

Conflicts of Interest: We declare that we do not have any commercial or associative interests in connection with the work submitted.

References

1. Luo, Y.; Zhang, Z.; Chhowalla, M.; Liu, B. Recent Advances in Design of Electrocatalysts for High-Current-Density Water Splitting. *Adv. Mater.* **2022**, *34*, 2108133. [[CrossRef](#)]
2. Saad, A.; Gao, Y.; Owusu, K.A.; Liu, W.; Wu, Y.; Ramiere, A.; Guo, H.; Tsiakaras, P.; Cai, X. Ternary Mo_2NiB_2 as a Superior Bifunctional Electrocatalyst for Overall Water Splitting. *Small* **2022**, *18*, 2104303. [[CrossRef](#)] [[PubMed](#)]
3. Riyajuddin, S.; Azmi, K.; Pahuja, M.; Kumar, S.; Maruyama, T.; Bera, C.; Ghosh, K. Super-Hydrophilic Hierarchical Ni-Foam-Graphene-Carbon Nanotubes- Ni_2P-CuP_2 Nano-Architecture as Efficient Electrocatalyst for Overall Water Splitting. *ACS Nano* **2021**, *15*, 5586–5599. [[CrossRef](#)]
4. Ifkovits, Z.P.; Evans, J.M.; Meier, M.C.; Papadantonakis, K.M.; Lewis, N.S. Decoupled Electrochemical Water-Splitting Systems: A Review and Perspective. *Energy Environ. Sci.* **2021**, *14*, 4740–4759. [[CrossRef](#)]

5. Guan, D.; Wang, B.; Zhang, J.; Shi, R.; Jiao, K.; Li, L.; Wang, Y.; Xie, B.; Zhang, Q.; Yu, J.; et al. Hydrogen Society: From Present to Future. *Energy Environ. Sci.* **2023**, *16*, 4926–4943. [[CrossRef](#)]
6. Yue, Q.; Sun, J.; Chen, S.; Zhou, Y.; Li, H.; Chen, Y.; Zhang, R.; Wei, G.; Kang, Y. Hierarchical Mesoporous MXene-NiCoP Electrocatalyst for Water-Splitting. *ACS Appl. Mater. Interfaces* **2020**, *12*, 18570–18577. [[CrossRef](#)]
7. Debata, S.; Patra, S.; Banerjee, S.; Madhuri, R.; Sharma, P.K. Controlled Hydrothermal Synthesis of Graphene Supported NiCo₂O₄ Coral-like Nanostructures: An Efficient Electrocatalyst for Overall Water Splitting. *Appl. Surf. Sci.* **2018**, *449*, 203–212. [[CrossRef](#)]
8. Kumaravel, S.; Karthick, K.; Sam Sankar, S.; Karmakar, A.; Madhu, R.; Bera, K.; Kundu, S. Recent Progresses in Engineering of Ni and Co Based Phosphides for Effective Electrocatalytic Water Splitting. *ChemElectroChem* **2021**, *8*, 4638–4685. [[CrossRef](#)]
9. Habib, M.A.; Mandavkar, R.; Lin, S.; Burse, S.; Khalid, T.; Joni, M.H.; Jeong, J.-H.; Lee, J. Ni-BP Micro Spheres for Superior Water Splitting OER Electrocatalyst Satisfying Industrial Operational Requirement. *Chem. Eng. J.* **2023**, *462*, 142177.
10. Battiato, S.; Bruno, L.; Pellegrino, A.L.; Terrasi, A.; Mirabella, S. Optimized Electroless Deposition of NiCoP Electrocatalysts for Enhanced Water Splitting. *Catal. Today* **2023**, *423*, 113929. [[CrossRef](#)]
11. Sun, H.; Xu, X.; Kim, H.; Shao, Z.; Jung, W. Advanced Electrocatalysts with Unusual Active Sites for Electrochemical Water Splitting. *InfoMat* **2024**, *6*, e12494. [[CrossRef](#)]
12. Loni, E.; Shokuhfar, A.; Siadati, M.H. Cobalt-Based Electrocatalysts for Water Splitting: An Overview. *Catal. Surv. Asia* **2021**, *25*, 114–147. [[CrossRef](#)]
13. Hu, E.; Feng, Y.; Nai, J.; Zhao, D.; Hu, Y.; Lou, X.W. Construction of Hierarchical Ni-Co-P Hollow Nanobricks with Oriented Nanosheets for Efficient Overall Water Splitting. *Energy Environ. Sci.* **2018**, *11*, 872–880. [[CrossRef](#)]
14. Burse, S.; Kulkarni, R.; Mandavkar, R.; Habib, M.A.; Lin, S.; Chung, Y.-U.; Jeong, J.-H.; Lee, J. Vanadium-Doped FeBP Microsphere Croissant for Significantly Enhanced Bi-Functional HER and OER Electrocatalyst. *Nanomaterials* **2022**, *12*, 3283. [[CrossRef](#)] [[PubMed](#)]
15. Barati Darband, G.; Aliofkhaezrai, M.; Rouhaghdam, A.S. Facile Electrodeposition of Ternary Ni-Fe-Co Alloy Nanostructure as a Binder Free, Cost-Effective and Durable Electrocatalyst for High-Performance Overall Water Splitting. *J. Colloid Interface Sci.* **2019**, *547*, 407–420. [[CrossRef](#)]
16. Meena, A.; Thangavel, P.; Jeong, D.S.; Singh, A.N.; Jana, A.; Im, H.; Nguyen, D.A.; Kim, K.S. Crystalline-Amorphous Interface of Mesoporous Ni₂P@FePO_xH_y for Oxygen Evolution at High Current Density in Alkaline-Anion-Exchange-Membrane Water-Electrolyzer. *Appl. Catal. B Environ.* **2022**, *306*, 121127. [[CrossRef](#)]
17. Mohili, R.; Hemanth, N.R.; Jin, H.; Lee, K.; Chaudhari, N. Emerging High Entropy Metal Sulphides and Phosphides for Electrochemical Water Splitting. *J. Mater. Chem. A* **2023**, *11*, 10463–10472. [[CrossRef](#)]
18. Wang, Z.; Liu, H.; Ge, R.; Ren, X.; Ren, J.; Yang, D.; Zhang, L.; Sun, X. Phosphorus-Doped Co₃O₄ Nanowire Array: A Highly Efficient Bifunctional Electrocatalyst for Overall Water Splitting. *ACS Catal.* **2018**, *8*, 2236–2241. [[CrossRef](#)]
19. Liu, H.; Li, X.; Ge, L.; Peng, C.; Zhu, L.; Zou, W.; Chen, J.; Wu, Q.; Zhang, Y.; Huang, H.; et al. Accelerating Hydrogen Evolution in Ru-Doped FeCoP Nanoarrays with Lattice Distortion toward Highly Efficient Overall Water Splitting. *Catal. Sci. Technol.* **2020**, *10*, 8314–8324. [[CrossRef](#)]
20. Wu, Y.; Gao, Y.; He, H.; Zhang, P. Novel Electrocatalyst of Nickel Sulfide Boron Coating for Hydrogen Evolution Reaction in Alkaline Solution. *Appl. Surf. Sci.* **2019**, *480*, 689–696. [[CrossRef](#)]
21. Zhao, D.; Wang, Y.; Dong, C.-L.; Huang, Y.-C.; Chen, J.; Xue, F.; Shen, S.; Guo, L. Boron-Doped Nitrogen-Deficient Carbon Nitride-Based Z-Scheme Heterostructures for Photocatalytic Overall Water Splitting. *Nat. Energy* **2021**, *6*, 388–397. [[CrossRef](#)]
22. Habib, M.A.; Mandavkar, R.; Burse, S.; Lin, S.; Kulkarni, R.; Patil, C.S.; Jeong, J.-H.; Lee, J. Design of Boron-Based Ternary W₃CoB₃ Electrocatalyst for the Improved HER and OER Performances. *Mater. Today Energy* **2022**, *26*, 101021. [[CrossRef](#)]
23. Nyarige, J.S.; Krüger, T.P.J.; Diale, M. Influence of Precursor Concentration and Deposition Temperature on the Photoactivity of Hematite Electrodes for Water Splitting. *Mater. Today Commun.* **2020**, *25*, 101459. [[CrossRef](#)]
24. Yang, W.; Wang, Z.; Zhang, W.; Guo, S. Electronic-Structure Tuning of Water-Splitting Nanocatalysts. *Trends Chem.* **2019**, *1*, 259–271. [[CrossRef](#)]
25. Xue, Y.; Sun, Y.; Wang, G.; Yan, K.; Zhao, J. Effect of NH₄F Concentration and Controlled-Charge Consumption on the Photocatalytic Hydrogen Generation of TiO₂ Nanotube Arrays. *Electrochim. Acta* **2015**, *155*, 312–320. [[CrossRef](#)]
26. Patil, S.J.; Chodankar, N.R.; Hwang, S.-K.; Rama Raju, G.S.; Huh, Y.-S.; Han, Y.-K. Fluorine Engineered Self-Supported Ultrathin 2D Nickel Hydroxide Nanosheets as Highly Robust and Stable Bifunctional Electrocatalysts for Oxygen Evolution and Urea Oxidation Reactions. *Small* **2022**, *18*, 2103326. [[CrossRef](#)]
27. Oliveira, F.G.S.; Santos, L.P.M.; da Silva, R.B.; Correa, M.A.; Bohn, F.; Correia, A.N.; Vieira, L.; Vasconcelos, I.F.; de Lima-Neto, P. Fe_xNi_(1-x) Coatings Electrodeposited from Choline Chloride-Urea Mixture: Magnetic and Electrocatalytic Properties for Water Electrolysis. *Mater. Chem. Phys.* **2022**, *279*, 125738. [[CrossRef](#)]
28. Liu, Y.; Yu, Y.; Mu, Z.; Wang, Y.; Ali, U.; Jing, S.; Xing, S. Urea-Assisted Enhanced Electrocatalytic Activity of MoS₂-Ni₃S₂ for Overall Water Splitting. *Inorg. Chem. Front.* **2020**, *7*, 3588–3597. [[CrossRef](#)]
29. Xu, T.; Yang, L.; Li, J.; Usoltseva, N.; An, V.; Jin, X.; Zhang, C.; Zhang, X.; Liu, B. NH₄F-Induced Morphology Control of CoP Nanostructures to Enhance the Hydrogen Evolution Reaction. *Inorg. Chem.* **2021**, *60*, 10781–10790. [[CrossRef](#)]
30. Jiang, Y.; Lu, Y. Designing Transition-Metal-Boride-Based Electrocatalysts for Applications in Electrochemical Water Splitting. *Nanoscale* **2020**, *12*, 9327–9351. [[CrossRef](#)]

31. Chen, L.; Ren, J.-T.; Yuan, Z.-Y. Design Strategies of Phosphorus-Containing Catalysts for Photocatalytic, Photoelectrochemical and Electrocatalytic Water Splitting. *Green Chem.* **2022**, *24*, 713–747. [[CrossRef](#)]
32. Wang, Y.; Gong, W.; Zuo, P.; Kang, L.; Yin, G. A Novel Spherical Boron Phosphide as a High-Efficiency Overall Water Splitting Catalyst: A Density Functional Theory Study. *Catal. Lett.* **2020**, *150*, 544–554. [[CrossRef](#)]
33. Wang, H.; Zou, H.; Liu, Y.; Liu, Z.; Sun, W.; Lin, K.A.; Li, T.; Luo, S. Ni₂P Nanocrystals Embedded Ni-MOF Nanosheets Supported on Nickel Foam as Bifunctional Electrocatalyst for Urea Electrolysis. *Sci. Rep.* **2021**, *11*, 21414. [[CrossRef](#)] [[PubMed](#)]
34. Foroughi, F.; Faid, A.Y.; Sunde, S.; Pollet, B.G. Sonoactivated Polycrystalline Ni Electrodes for Alkaline Oxygen Evolution Reaction. *Ultrason. Sonochem.* **2022**, *86*, 106013. [[CrossRef](#)]
35. Lin, S.; Habib, M.A.; Mandavkar, R.; Kulkarni, R.; Burse, S.; Chung, Y.-U.; Liu, C.; Wang, Z.; Lin, S.; Jeong, J.-H.; et al. Higher Water-Splitting Performance of Boron-Based Porous CoMnB Electrocatalyst over the Benchmarks at High Current in 1 m KOH and Real Sea Water. *Adv. Sustain. Syst.* **2022**, *6*, 2200213. [[CrossRef](#)]
36. Chen, X.; Jiang, R.; Dong, C.; Liu, H.; Yang, J.; Du, X. Polycrystalline CoO-Co₉S₈ Heterostructure Nanoneedle Arrays as Bifunctional Catalysts for Efficient Overall Water Splitting. *ChemElectroChem* **2022**, *9*, e202101566. [[CrossRef](#)]
37. Guo, C.; Shi, Y.; Lu, S.; Yu, Y.; Zhang, B. Amorphous Nanomaterials in Electrocatalytic Water Splitting. *Chin. J. Catal.* **2021**, *42*, 1287–1296. [[CrossRef](#)]
38. Xu, Y.; Tu, W.; Zhang, B.; Yin, S.; Huang, Y.; Kraft, M.; Xu, R. Nickel Nanoparticles Encapsulated in Few-Layer Nitrogen-Doped Graphene Derived from Metal–Organic Frameworks as Efficient Bifunctional Electrocatalysts for Overall Water Splitting. *Adv. Mater.* **2017**, *29*, 1605957. [[CrossRef](#)]
39. Makimizu, Y.; Yoo, J.; Poornajar, M.; Nguyen, N.T.; Ahn, H.-J.; Hwang, I.; Kment, S.; Schmuki, P. Effects of Low Oxygen Annealing on the Photoelectrochemical Water Splitting Properties of α -Fe₂O₃. *J. Mater. Chem. A* **2020**, *8*, 1315–1325. [[CrossRef](#)]
40. Mandavkar, R.; Habib, M.A.; Lin, S.; Kulkarni, R.; Burse, S.; Jeong, J.-H.; Lee, J. Electron Enriched Ternary NiMoB Electrocatalyst for Improved Overall Water Splitting: Better Performance as Compared to the Pt/C || RuO₂ at High Current Density. *Appl. Mater. Today* **2022**, *29*, 101579. [[CrossRef](#)]
41. Diaz-Morales, O.; Ferrus-Suspedra, D.; Koper, M.T.M. The Importance of Nickel Oxyhydroxide Deprotonation on Its Activity towards Electrochemical Water Oxidation. *Chem. Sci.* **2016**, *7*, 2639–2645. [[CrossRef](#)] [[PubMed](#)]
42. Huang, C.; Zhang, B.; Wu, Y.; Ruan, Q.; Liu, L.; Su, J.; Tang, Y.; Liu, R.; Chu, P.K. Experimental and Theoretical Investigation of Reconstruction and Active Phases on Honeycombed Ni₃N-Co₃N/C in Water Splitting. *Appl. Catal. B Environ.* **2021**, *297*, 120461. [[CrossRef](#)]
43. Guo, M.; Meng, H.; Jin, J.; Mi, J. Amine-Assisted Synthesis of the Ni₃Fe Alloy Encapsulated in Nitrogen-Doped Carbon for High-Performance Water Splitting. *J. Mater. Chem. A* **2023**, *11*, 6452–6464. [[CrossRef](#)]
44. Chastain, J.; King, R.C., Jr. *Handbook of X-ray Photoelectron Spectroscopy*; Perkin-Elmer Corp.: Waltham, MA, USA, 1992; Volume 40, p. 221.
45. Guo, T.; Chen, L.; Li, Y.; Shen, K. Controllable Synthesis of Ultrathin Defect-Rich LDH Nanoarrays Coupled with MOF-Derived Co-NC Microarrays for Efficient Overall Water Splitting. *Small* **2022**, *18*, 2107739. [[CrossRef](#)] [[PubMed](#)]
46. Biesinger, M.C.; Payne, B.P.; Grosvenor, A.P.; Lau, L.W.M.; Gerson, A.R.; Smart, R.S.C. Resolving Surface Chemical States in XPS Analysis of First Row Transition Metals, Oxides and Hydroxides: Cr, Mn, Fe, Co and Ni. *Appl. Surf. Sci.* **2011**, *257*, 2717–2730. [[CrossRef](#)]
47. Li, C.-F.; Zhao, J.-W.; Xie, L.-J.; Wu, J.-Q.; Li, G.-R. Fe Doping and Oxygen Vacancy Modulated Fe-Ni₅P₄/NiFeOH Nanosheets as Bifunctional Electrocatalysts for Efficient Overall Water Splitting. *Appl. Catal. B Environ.* **2021**, *291*, 119987. [[CrossRef](#)]
48. Teng, W.; Huo, M.; Sun, Z.; Yang, W.; Zheng, X.; Ding, C.; Zhang, S. FeCoNi Sulfides Derived from in Situ Sulfurization of Precursor Oxides as Oxygen Evolution Reaction Catalyst. *Front. Chem.* **2020**, *8*, 334. [[CrossRef](#)] [[PubMed](#)]
49. Hou, Z.; Yan, P.; Sun, B.; Elshekh, H.; Yan, B. An Excellent Soft Magnetic Fe/Fe₃O₄-FeSiAl Composite with High Permeability and Low Core Loss. *Results Phys.* **2019**, *14*, 102498. [[CrossRef](#)]
50. Li, X.; Xiao, L.; Zhou, L.; Xu, Q.; Weng, J.; Xu, J.; Liu, B. Adaptive Bifunctional Electrocatalyst of Amorphous CoFe Oxide @ 2D Black Phosphorus for Overall Water Splitting. *Angew. Chem.* **2020**, *132*, 21292–21299. [[CrossRef](#)]
51. Hao, W.; Yao, D.; Xu, Q.; Wang, R.; Zhang, C.; Guo, Y.; Sun, R.; Huang, M.; Chen, Z. Highly Efficient Overall-Water Splitting Enabled via Grafting Boron-Inserted Fe-Ni Solid Solution Nanosheets onto Unconventional Skeleton. *Appl. Catal. B Environ.* **2021**, *292*, 120188. [[CrossRef](#)]
52. Wei, Y.; Zou, P.; Yue, Y.; Wang, M.; Fu, W.; Si, S.; Wei, L.; Zhao, X.; Hu, G.; Xin, H.L. One-Pot Synthesis of B/P-Codoped Co-Mo Dual-Nanowafer Electrocatalysts for Overall Water Splitting. *ACS Appl. Mater. Interfaces* **2021**, *13*, 20024–20033. [[CrossRef](#)] [[PubMed](#)]
53. Anantharaj, S.; Noda, S.; Driess, M.; Menezes, P.W. The Pitfalls of Using Potentiodynamic Polarization Curves for Tafel Analysis in Electrocatalytic Water Splitting. *ACS Energy Lett.* **2021**, *6*, 1607–1611. [[CrossRef](#)]
54. Peng, Y.; Mak, C.H.; Kai, J.-J.; Du, M.; Ji, L.; Yuan, M.; Zou, X.; Shen, H.-H.; Santoso, S.P.; Colmenares, J.C.; et al. Recent Progress on Post-Synthetic Treatments of Photoelectrodes for Photoelectrochemical Water Splitting. *J. Mater. Chem. A* **2021**, *9*, 26628–26649. [[CrossRef](#)]
55. Zhang, H.; Guan, D.; Gu, Y.; Xu, H.; Wang, C.; Shao, Z.; Guo, Y. Tuning Synergy between Nickel and Iron in Ruddlesden–Popper Perovskites through Controllable Crystal Dimensionalities towards Enhanced Oxygen-evolving Activity and Stability. *Carbon Energy* **2024**, e465. [[CrossRef](#)]

56. Al-Naggar, A.H.; Shinde, N.M.; Kim, J.-S.; Mane, R.S. Water Splitting Performance of Metal and Non-Metal-Doped Transition Metal Oxide Electrocatalysts. *Coord. Chem. Rev.* **2023**, *474*, 214864. [[CrossRef](#)]
57. Yuan, W.; Wang, S.; Ma, Y.; Qiu, Y.; An, Y.; Cheng, L. Interfacial Engineering of Cobalt Nitrides and Mesoporous Nitrogen-Doped Carbon: Toward Efficient Overall Water-Splitting Activity with Enhanced Charge-Transfer Efficiency. *ACS Energy Lett.* **2020**, *5*, 692–700. [[CrossRef](#)]
58. Hu, C.; Zhang, L.; Gong, J. Recent Progress Made in the Mechanism Comprehension and Design of Electrocatalysts for Alkaline Water Splitting. *Energy Environ. Sci.* **2019**, *12*, 2620–2645. [[CrossRef](#)]
59. Shalom, M.; Ressnig, D.; Yang, X.; Clavel, G.; Fellinger, T.P.; Antonietti, M. Nickel Nitride as an Efficient Electrocatalyst for Water Splitting. *J. Mater. Chem. A* **2015**, *3*, 8171–8177. [[CrossRef](#)]
60. Xu, S.; Zhao, H.; Li, T.; Liang, J.; Lu, S.; Chen, G.; Gao, S.; Asiri, A.M.; Wu, Q.; Sun, X. Iron-Based Phosphides as Electrocatalysts for the Hydrogen Evolution Reaction: Recent Advances and Future Prospects. *J. Mater. Chem. A* **2020**, *8*, 19729–19745. [[CrossRef](#)]
61. Gupta, S.; Patel, M.K.; Miotello, A.; Patel, N. Metal Boride-Based Catalysts for Electrochemical Water-Splitting: A Review. *Adv. Funct. Mater.* **2020**, *30*, 1906481. [[CrossRef](#)]
62. Jeong, J.H.; Kunwar, S.; Pandit, S.; Lee, J. CoP₂Nanoparticles Deposited on Nanometer-Thick Pt-Coated Fluorine-Doped Tin Oxide Substrates as Electrocatalysts for Simultaneous Hydrogen Evolution and Oxygen Evolution. *ACS Appl. Nano Mater.* **2020**, *3*, 6507–6515. [[CrossRef](#)]
63. Anantharaj, S.; Kundu, S. Do the Evaluation Parameters Reflect Intrinsic Activity of Electrocatalysts in Electrochemical Water Splitting? *ACS Energy Lett.* **2019**, *4*, 1260–1264. [[CrossRef](#)]
64. Wang, S.; Lu, A.; Zhong, C.-J. Hydrogen Production from Water Electrolysis: Role of Catalysts. *Nano Converg.* **2021**, *8*, 4. [[CrossRef](#)] [[PubMed](#)]
65. Yao, Y.; Zhang, Z.; Jiao, L. Development Strategies in Transition Metal Borides for Electrochemical Water Splitting. *Energy Environ. Mater.* **2022**, *5*, 470–485. [[CrossRef](#)]
66. Bahadur, A.; Hussain, W.; Iqbal, S.; Ullah, F.; Shoaib, M.; Liu, G.; Feng, K. A Morphology Controlled Surface Sulfurized CoMn₂O₄ Microspike Electrocatalyst for Water Splitting with Excellent OER Rate for Binder-Free Electrocatalytic Oxygen Evolution. *J. Mater. Chem. A* **2021**, *9*, 12255–12264. [[CrossRef](#)]
67. Friebel, D.; Bajdich, M.; Yeo, B.S.; Louie, M.W.; Miller, D.J.; Sanchez Casalongue, H.; Mbuga, F.; Weng, T.-C.; Nordlund, D.; Sokaras, D.; et al. On the Chemical State of Co Oxide Electrocatalysts during Alkaline Water Splitting. *Phys. Chem. Chem. Phys.* **2013**, *15*, 17460–17467. [[CrossRef](#)] [[PubMed](#)]
68. Behl, W.K.; Toni, J.E. Anodic Oxidation of Cobalt in Potassium Hydroxide Electrolytes. *J. Electroanal. Chem. Interfacial Electrochem.* **1971**, *31*, 63–75. [[CrossRef](#)]
69. Shit, S.; Bolar, S.; Murmu, N.C.; Kuila, T. An Account of the Strategies to Enhance the Water Splitting Efficiency of Noble-Metal-Free Electrocatalysts. *J. Energy Chem.* **2021**, *59*, 160–190. [[CrossRef](#)]
70. Tian, L.; Li, Z.; Xu, X.; Zhang, C. Advances in Noble Metal (Ru, Rh, and Ir) Doping for Boosting Water Splitting Electrocatalysis. *J. Mater. Chem. A* **2021**, *9*, 13459–13470. [[CrossRef](#)]
71. Hausmann, J.N.; Menezes, P.W. Why Should Transition Metal Chalcogenides Be Investigated as Water Splitting Precatalysts Even Though They Transform into (Oxyhydr)Oxides? *Curr. Opin. Electrochem.* **2022**, *34*, 100991. [[CrossRef](#)]
72. Wang, D.; Li, Q.; Han, C.; Lu, Q.; Xing, Z.; Yang, X. Atomic and Electronic Modulation of Self-Supported Nickel-Vanadium Layered Double Hydroxide to Accelerate Water Splitting Kinetics. *Nat. Commun.* **2019**, *10*, 3899. [[CrossRef](#)] [[PubMed](#)]
73. Ashraf, M.A.; Li, C.; Pham, B.T.; Zhang, D. Electrodeposition of Ni–Fe–Mn Ternary Nanosheets as Affordable and Efficient Electrocatalyst for Both Hydrogen and Oxygen Evolution Reactions. *Int. J. Hydrogen Energy* **2020**, *45*, 24670–24683. [[CrossRef](#)]
74. Lu, W.; Liu, T.; Xie, L.; Tang, C.; Liu, D.; Hao, S.; Qu, F.; Du, G.; Ma, Y.; Asiri, A.M.; et al. In Situ Derived Co—B Nanoarray: A High-Efficiency and Durable 3D Bifunctional Electrocatalyst for Overall Alkaline Water Splitting. *Small* **2017**, *13*, 1700805. [[CrossRef](#)]
75. Liu, Y.; Cao, J.; Chen, Y.; Wei, M.; Liu, X.; Li, X.; Wu, Q.; Feng, B.; Zhang, Y.; Yang, L. Regulation of the Morphology and Electrochemical Properties of Ni_{0.85}Se via Fe Doping for Overall Water Splitting and Supercapacitors. *CrystEngComm* **2022**, *24*, 1704–1718. [[CrossRef](#)]
76. Shit, S.; Bolar, S.; Murmu, N.C.; Kuila, T. Binder-Free Growth of Nickel-Doped Iron Sulfide on Nickel Foam via Electrochemical Deposition for Electrocatalytic Water Splitting. *ACS Sustain. Chem. Eng.* **2019**, *7*, 18015–18026. [[CrossRef](#)]
77. Wang, J.; Zhang, M.; Yang, G.; Song, W.; Zhong, W.; Wang, X.; Wang, M.; Sun, T.; Tang, Y. Heterogeneous Bimetallic Mo–NiP_x/NiS_y as a Highly Efficient Electrocatalyst for Robust Overall Water Splitting. *Adv. Funct. Mater.* **2021**, *31*, 2101532. [[CrossRef](#)]
78. Kong, D.; Wang, Y.; Huang, S.; Von Lim, Y.; Wang, M.; Xu, T.; Zang, J.; Li, X.; Yang, H.Y. Defect-Engineered 3D Hierarchical NiMo₃S₄ Nanoflowers as Bifunctional Electrocatalyst for Overall Water Splitting. *J. Colloid Interface Sci.* **2022**, *607*, 1876–1887. [[CrossRef](#)]
79. Abdelghafar, F.; Xu, X.; Jiang, S.P.; Shao, Z. Perovskite for Electrocatalytic Oxygen Evolution at Elevated Temperatures. *ChemSusChem* **2024**, e202301534. [[CrossRef](#)]
80. Li, H.; Yang, S.; Wei, W.; Zhang, M.; Jiang, Z.; Yan, Z.; Xie, J. Chrysanthemum-like FeS/Ni₃S₂ Heterostructure Nanoarray as a Robust Bifunctional Electrocatalyst for Overall Water Splitting. *J. Colloid Interface Sci.* **2022**, *608*, 536–548. [[CrossRef](#)]
81. Ren, G.; Hao, Q.; Mao, J.; Liang, L.; Liu, H.; Liu, C.; Zhang, J. Ultrafast Fabrication of Nickel Sulfide Film on Ni Foam for Efficient Overall Water Splitting. *Nanoscale* **2018**, *10*, 17347–17353. [[CrossRef](#)]

82. Chen, M.-T.; Duan, J.-J.; Feng, J.-J.; Mei, L.-P.; Jiao, Y.; Zhang, L.; Wang, A.-J. Iron, Rhodium-Codoped Ni₂P Nanosheets Arrays Supported on Nickel Foam as an Efficient Bifunctional Electrocatalyst for Overall Water Splitting. *J. Colloid Interface Sci.* **2022**, *605*, 888–896. [[CrossRef](#)] [[PubMed](#)]
83. Wu, Y.; Li, Y.; Yuan, M.; Hao, H.; San, X.; Lv, Z.; Xu, L.; Wei, B. Operando Capturing of Surface Self-Reconstruction of Ni₃S₂/FeNi₂S₄ Hybrid Nanosheet Array for Overall Water Splitting. *Chem. Eng. J.* **2022**, *427*, 131944. [[CrossRef](#)]
84. Alaghmandfar, A.; Ghandi, K. A Comprehensive Review of Graphitic Carbon Nitride (g-C₃N₄)-Metal Oxide-Based Nanocomposites: Potential for Photocatalysis and Sensing. *Nanomaterials* **2022**, *12*, 294. [[CrossRef](#)] [[PubMed](#)]
85. Yang, M.; Zhao, M.; Yuan, J.; Luo, J.; Zhang, J.; Lu, Z.; Chen, D.; Fu, X.; Wang, L.; Liu, C. Oxygen Vacancies and Interface Engineering on Amorphous/Crystalline CrOx-Ni₃N Heterostructures toward High-Durability and Kinetically Accelerated Water Splitting. *Small* **2022**, *18*, 2106554. [[CrossRef](#)]
86. Anantharaj, S.; Noda, S. Amorphous Catalysts and Electrochemical Water Splitting: An Untold Story of Harmony. *Small* **2020**, *16*, 1905779. [[CrossRef](#)]
87. Browne, M.P.; Vasconcelos, J.M.; Coelho, J.; O'Brien, M.; Rovetta, A.A.; McCarthy, E.K.; Nolan, H.; Duesberg, G.S.; Nicolosi, V.; Colavita, P.E.; et al. Improving the Performance of Porous Nickel Foam for Water Oxidation Using Hydrothermally Prepared Ni and Fe Metal Oxides. *Sustain. Energy Fuels* **2017**, *1*, 207–216. [[CrossRef](#)]
88. Anantharaj, S.; Ede, S.R.; Karthick, K.; Sam Sankar, S.; Sangeetha, K.; Karthik, P.E.; Kundu, S. Precision and Correctness in the Evaluation of Electrocatalytic Water Splitting: Revisiting Activity Parameters with a Critical Assessment. *Energy Environ. Sci.* **2018**, *11*, 744–771. [[CrossRef](#)]
89. Feng, R.; Zhu, Q.; Chu, M.; Jia, S.; Zhai, J.; Wu, H.; Wu, P.; Han, B. Electrodeposited Cu–Pd Bimetallic Catalysts for the Selective Electroreduction of CO₂ to Ethylene. *Green Chem.* **2020**, *22*, 7560–7565. [[CrossRef](#)]
90. Han, A.; Chen, H.; Sun, Z.; Xu, J.; Du, P. High Catalytic Activity for Water Oxidation Based on Nanostructured Nickel Phosphide Precursors. *Chem. Commun.* **2015**, *51*, 11626–11629. [[CrossRef](#)]
91. Wang, G.; Hua, C.; Chen, W.; Fan, H.; Feng, P.; Zhu, Y. Intriguing 3D Micro-Flower Structure of Co_{1.11}Te₂ Deposited on Te Nanosheets Showing an Efficient Bifunctional Electrocatalytic Property for Overall Water Splitting. *Electrochim. Acta* **2023**, *447*, 142133. [[CrossRef](#)]
92. Sun, H.; Meng, J.; Jiao, L.; Cheng, F.; Chen, J. A Review of Transition-Metal Boride/Phosphide-Based Materials for Catalytic Hydrogen Generation from Hydrolysis of Boron-Hydrides. *Inorg. Chem. Front.* **2018**, *5*, 760–772. [[CrossRef](#)]
93. Yang, G.; Jiao, Y.; Yan, H.; Xie, Y.; Wu, A.; Dong, X.; Guo, D.; Tian, C.; Fu, H. Interfacial Engineering of MoO₂-FeP Heterojunction for Highly Efficient Hydrogen Evolution Coupled with Biomass Electrooxidation. *Adv. Mater.* **2020**, *32*, 2000455. [[CrossRef](#)] [[PubMed](#)]
94. Feng, J.; Wang, X.; Zhang, D.; Wang, Y.; Wang, J.; Pi, M.; Zhou, H.; Li, J.; Chen, S. Porous Mn-Doped CoP₃ Nanowires as a Janus Electrocatalyst for Efficient Overall Water Splitting in Alkaline Solution. *J. Electrochem. Soc.* **2018**, *165*, F1323. [[CrossRef](#)]
95. Yu, X.; Yu, Z.-Y.; Zhang, X.-L.; Li, P.; Sun, B.; Gao, X.; Yan, K.; Liu, H.; Duan, Y.; Gao, M.-R.; et al. Highly Disordered Cobalt Oxide Nanostructure Induced by Sulfur Incorporation for Efficient Overall Water Splitting. *Nano Energy* **2020**, *71*, 104652. [[CrossRef](#)]
96. Wang, X.; Huang, H.; Qian, J.; Li, Y.; Shen, K. Intensified Kirkendall Effect Assisted Construction of Double-Shell Hollow Cu-Doped CoP Nanoparticles Anchored by Carbon Arrays for Water Splitting. *Appl. Catal. B Environ.* **2023**, *325*, 122295. [[CrossRef](#)]
97. Wang, L.; Lu, X.; Han, C.; Lu, R.; Yang, S.; Song, X. Electrospun Hollow Cage-like α-Fe₂O₃ Microspheres: Synthesis, Formation Mechanism, and Morphology-Preserved Conversion to Fe Nanostructures. *CrystEngComm* **2014**, *16*, 10618–10623. [[CrossRef](#)]
98. Zhang, H.; Lee, J.S. Hybrid Microwave Annealing Synthesizes Highly Crystalline Nanostructures for (Photo)Electrocatalytic Water Splitting. *Acc. Chem. Res.* **2019**, *52*, 3132–3142. [[CrossRef](#)]
99. Kim, T.; Roy, S.B.; Moon, S.; Yoo, S.; Choi, H.; Parale, V.G.; Kim, Y.; Lee, J.; Jun, S.C.; Kang, K. Highly Dispersed Pt Clusters on F-Doped Tin (IV) Oxide Aerogel Matrix: An Ultra-Robust Hybrid Catalyst for Enhanced Hydrogen Evolution. *ACS Nano* **2022**, *16*, 1625–1638. [[CrossRef](#)] [[PubMed](#)]
100. Liu, Y.; Li, H.; Gong, S.; Chen, Y.; Xie, R.; Wu, Q.; Tao, J.; Meng, F.; Zhao, P. A Novel Non-Enzymatic Electrochemical Biosensor Based on the Nanohybrid of Bimetallic PdCu Nanoparticles/Carbon Black for Highly Sensitive Detection of H₂O₂ Released from Living Cells. *Sens. Actuators B Chem.* **2019**, *290*, 249–257. [[CrossRef](#)]
101. Sultan, S.; Ha, M.; Kim, D.Y.; Tiwari, J.N.; Myung, C.W.; Meena, A.; Shin, T.J.; Chae, K.H.; Kim, K.S. Superb Water Splitting Activity of the Electrocatalyst Fe₃Co(PO₄)₄ Designed with Computation Aid. *Nat. Commun.* **2019**, *10*, 5195. [[CrossRef](#)]
102. Yang, J.; An, Y.; Guo, K.; Ren, X.; Jiang, B. Nitrogen Doped FeCoNiS Nanoparticles on N, S-Co-Doped Vertical Graphene as Bifunctional Electrocatalyst for Water Splitting. *Int. J. Hydrogen Energy* **2023**, *48*, 4143–4157. [[CrossRef](#)]
103. Surendran, S.; Jesudass, S.C.; Janani, G.; Kim, J.Y.; Lim, Y.; Park, J.; Han, M.-K.; Cho, I.S.; Sim, U. Sulphur Assisted Nitrogen-Rich CNF for Improving Electronic Interactions in Co-NiO Heterostructures toward Accelerated Overall Water Splitting. *Adv. Mater. Technol.* **2023**, *8*, 2200572. [[CrossRef](#)]
104. Miao, L.; Sui, L.; Shen, X.; Yang, D.; Huang, H.; Kuang, Y. Realizing High Performance Bifunctional Energy Storage Devices and Electrocatalytic Water Splitting Catalysts through Regulated Interface Engineering of ZnCo₂O₄@Co₃O₄ Nanosheets. *CrystEngComm* **2023**, *25*, 4812–4821. [[CrossRef](#)]
105. Tsai, F.-T.; Deng, Y.-T.; Pao, C.-W.; Chen, J.-L.; Lee, J.-F.; Lai, K.-T.; Liaw, W.-F. The HER/OER Mechanistic Study of an FeCoNi-Based Electrocatalyst for Alkaline Water Splitting. *J. Mater. Chem. A* **2020**, *8*, 9939–9950. [[CrossRef](#)]

106. Du, Y.; Li, Z.; Liu, H.; Qiao, S.; Chen, Y.; Zhu, Z.; Tang, Y.; Liu, C. Scalable Oxygen-Assisted-Fe²⁺ Etching Approach towards Amorphous/Crystalline Structure Fe-Ni₂P Nanoarray for Efficient Water Splitting. *J. Alloy. Compd.* **2023**, *936*, 168073. [[CrossRef](#)]
107. Yang, N.; Tian, S.; Feng, Y.; Hu, Z.; Liu, H.; Tian, X.; Xu, L.; Hu, C.; Yang, J. Introducing High-Valence Iridium Single Atoms into Bimetal Phosphides toward High-Efficiency Oxygen Evolution and Overall Water Splitting. *Small* **2023**, *19*, 2207253. [[CrossRef](#)]
108. Dai, Z.; Du, X.; Zhang, X. The Synthesis of Ni-Co-Fe-Se@NiCo-LDH Nanoarrays on Ni Foam as Efficient Overall Water Splitting Electrocatalyst. *J. Alloy. Compd.* **2023**, *946*, 169451. [[CrossRef](#)]
109. Chen, M.; Kitiphatpiboon, N.; Feng, C.; Zhao, Q.; Abudula, A.; Ma, Y.; Yan, K.; Guan, G. Tuning Octahedron Sites in MnFe₂O₄ Spinel by Boron Doping for Highly Efficient Seawater Splitting. *Appl. Catal. B Environ.* **2023**, *330*, 122577. [[CrossRef](#)]
110. Guo, F.; Li, W.; Liu, Y.; Chen, Q.; Zhong, Q. Heterogeneous Fe-Doped NiCoP-MoO₃ Efficient Electrocatalysts for Overall Water Splitting. *Langmuir* **2023**, *39*, 1042–1050. [[CrossRef](#)]
111. Lei, B.; Xu, D.; Wei, B.; Xie, T.; Xiao, C.; Jin, W.; Xu, L. In Situ Synthesis of α-Fe₂O₃/Fe₃O₄ Heterojunction Photoanode via Fast Flame Annealing for Enhanced Charge Separation and Water Oxidation. *ACS Appl. Mater. Interfaces* **2021**, *13*, 4785–4795. [[CrossRef](#)]
112. Wang, Y.; Yu, W.; Zhou, B.; Xiao, W.; Wang, J.; Wang, X.; Xu, G.; Li, B.; Li, Z.; Wu, Z.; et al. Corrosive Engineering Assisted in Situ Construction of an Fe-Ni-Based Compound for Industrial Overall Water-Splitting under Large-Current Density in Alkaline Freshwater and Seawater Media. *J. Mater. Chem. A* **2023**, *11*, 1886–1893. [[CrossRef](#)]
113. Xiao, Y.; Shen, Y.; Su, D.; Zhang, S.; Yang, J.; Yan, D.; Fang, S.; Wang, X. Engineering Cu_{1.96}S/Co₉S₈ with Sulfur Vacancy and Heterostructure as an Efficient Bifunctional Electrocatalyst for Water Splitting. *J. Mater. Sci. Technol.* **2023**, *154*, 1–8. [[CrossRef](#)]
114. He, B.; Wang, X.-C.; Xia, L.-X.; Guo, Y.-Q.; Tang, Y.-W.; Zhao, Y.; Hao, Q.-L.; Yu, T.; Liu, H.-K.; Su, Z. Metal-Organic Framework-Derived Fe-Doped Co_{1.11}Te₂ Embedded in Nitrogen-Doped Carbon Nanotube for Water Splitting. *ChemSusChem* **2020**, *13*, 5239–5247. [[CrossRef](#)]
115. Zhu, C.; Wang, A.-L.; Xiao, W.; Chao, D.; Zhang, X.; Tiep, N.H.; Chen, S.; Kang, J.; Wang, X.; Ding, J.; et al. In Situ Grown Epitaxial Heterojunction Exhibits High-Performance Electrocatalytic Water Splitting. *Adv. Mater.* **2018**, *30*, 1705516. [[CrossRef](#)]
116. Lv, J.; Liu, P.; Yang, F.; Xing, L.; Wang, D.; Chen, X.; Gao, H.; Huang, X.; Lu, Y.; Wang, G. 3D Hydrangea Macrophylla-like Nickel–Vanadium Metal–Organic Frameworks Formed by Self-Assembly of Ultrathin 2D Nanosheets for Overall Water Splitting. *ACS Appl. Mater. Interfaces* **2020**, *12*, 48495–48510. [[CrossRef](#)] [[PubMed](#)]
117. Huang, C.; Ouyang, T.; Zou, Y.; Li, N.; Liu, Z.-Q. Ultrathin NiCo₂P_x Nanosheets Strongly Coupled with CNTs as Efficient and Robust Electrocatalysts for Overall Water Splitting. *J. Mater. Chem. A* **2018**, *6*, 7420–7427. [[CrossRef](#)]
118. Ma, Y.; Zhou, Y.; Wang, C.; Gao, B.; Li, J.; Zhu, M.; Wu, H.; Zhang, C.; Qin, Y. Photothermal–Magnetic Synergistic Effects in an Electrocatalyst for Efficient Water Splitting under Optical–Magnetic Fields. *Adv. Mater.* **2023**, *35*, 2303741. [[CrossRef](#)] [[PubMed](#)]
119. Hong, C.-B.; Li, X.; Wei, W.-B.; Wu, X.-T.; Zhu, Q.-L. Nano-Engineering of Ru-Based Hierarchical Porous Nanoreactors for Highly Efficient PH-Universal Overall Water Splitting. *Appl. Catal. B Environ.* **2021**, *294*, 120230. [[CrossRef](#)]
120. Zhao, C.; Wang, J.; Gao, Y.; Zhang, J.; Huang, C.; Shi, Q.; Mu, S.; Xiao, Q.; Huo, S.; Xia, Z.; et al. D-Orbital Manipulated Ru Nanoclusters for High-Efficiency Overall Water Splitting at Industrial-Level Current Densities. *Adv. Funct. Mater.* **2023**, *34*, 2307917. [[CrossRef](#)]
121. Nagappan, S.; Karmakar, A.; Madhu, R.; Dhandapani, H.N.; Singha Roy, S.; Kundu, S. Tuning the Active Sites and Optimizing the D-Spacing Value in CoFe-LDH by Ex Situ Intercalation of Guest Anions: An Innovative Electrocatalyst for Overall Water Splitting Reaction. *Catal. Sci. Technol.* **2023**, *13*, 6377–6391. [[CrossRef](#)]

Disclaimer/Publisher’s Note: The statements, opinions and data contained in all publications are solely those of the individual author(s) and contributor(s) and not of MDPI and/or the editor(s). MDPI and/or the editor(s) disclaim responsibility for any injury to people or property resulting from any ideas, methods, instructions or products referred to in the content.